Bed topography and the development of forced bed surface patches

Peter A. Nelson,[1] William E. Dietrich,[1] and Jeremy G. Venditti[2]

Received 15 April 2010; revised 25 August 2010; accepted 1 September 2010; published 24 November 2010.

[1] Channel topography in gravel-bedded rivers interacts with the local flow and sediment transport fields to produce "forced patches," which are temporally stable areas on the bed that display similar grain size and sorting. In an effort to enhance our empirical understanding of the mechanisms responsible for the formation of forced patches, we conducted a near-field scale flume experiment in which a large (55 m long, 2.74 m wide), straight, sediment recirculating flume was provided a constant water discharge and a unimodal sediment mixture ranging in size from 2 to 45 mm. A sequence of alternate bars developed and became essentially fixed in space, producing quasi-steady state bed topography over which we made measurements of local near-bed velocity and sediment transport. The bed developed temporally and spatially persistent forced patches with a general pattern of coarse bar tops and fine pools, which we characterized by visual mapping and with the application of an automated image processing procedure to a high-resolution (1 × 1 mm) digital elevation model of the bed surface. The boundary shear stress field, calculated from velocity measurements and with a quasi-three-dimensional hydraulic model (FaSTMECH), displayed substantial variability across the bar unit. Bed surface grain size did not correlate with local boundary shear stress; instead, topographically forced divergences in the boundary shear stress field were matched by divergences in the sediment transport field. The resultant cross-stream sediment flux was size-selective that in turn forced a bed surface textural response leading to coarse bar tops and fine pools. Our observations suggest that size-selective cross-stream bed load transport is a mechanism responsible for the development of forced bed surface patches in gravel bed channels that have topographically forced heterogeneous flow fields.

Citation: Nelson, P. A., W. E. Dietrich, and J. G. Venditti (2010), Bed topography and the development of forced bed surface patches, *J. Geophys. Res.*, *115*, F04024, doi:10.1029/2010JF001747.

1. Introduction

[2] A striking characteristic of most rivers is the patchy nature of their beds. That is, the sediment mixture comprising the channel bed becomes sorted into areas of similar grain size, producing discrete patches of a mappable scale [e.g., *Bluck*, 1971; *Bridge and Jarvis*, 1976; *Forbes*, 1983; *Dietrich and Smith*, 1984; *Kinerson*, 1990; *Wolcott and Church*, 1991; *Lisle and Madej*, 1992; *Paola and Seal*, 1995; *Sambrook Smith and Ferguson*, 1995; *Crowder and Diplas*, 1997; *Buffington and Montgomery*, 1999a; *Dietrich et al.*, 2005; *Yarnell et al.*, 2006; *Nelson et al.*, 2009]. Field studies suggest that some patches remain in a fixed location for an extended period even after passing considerable bed load flux [*Dietrich et al.*, 2005] while others are able to migrate downstream as, for example, bed load sheets [*Whiting et al.*, 1988; *Nelson et al.*, 2009, and references therein]. This variety of patch types led *Nelson et al.* [2009] to classify end-member patch types as "free" (downstream migrating sorting features), "fixed" (spatially persistent due to weak, grain scale, topographic controls and local coarsening), and "forced" (spatially persistent due to strong topographic controls such as bar morphology and channel obstructions).

[3] Free patches can be difficult to observe because they occur during periods of high flow and active transport. Forced patches, however, are spatially persistent and observable at low flow, which some have suggested is diagnostic of high-transport conditions [e.g., *Andrews and Erman*, 1986; *Wilcock and DeTemple*, 2005; *Clayton and Pitlick*, 2008]. Forced patches occur in virtually all channel morphologies. Strong, persistent sorting patterns are typical of river bends, in which inner point bars tend to be finer than outer pools, with the coarsest bed sediment shifting from the inside to the outside the bend [*Bluck*, 1971; *Jackson*, 1975; *Bridge and Jarvis*, 1976, 1982; *Dietrich and Smith*, 1983, 1984; *Carson*, 1986; *Whiting and Dietrich*, 1991; *Laronne and Duncan*, 1992; *Whiting*, 1996; *Clayton and Pitlick*, 2008; *Clayton*, 2010]. Straight channels with riffle-pool sequences typically have coarse riffles and fine pools [*Gilbert*, 1914;

[1]Department of Earth and Planetary Science, University of California, Berkeley, California, USA.
[2]Department of Geography, Simon Fraser University, Burnaby, British Columbia, Canada.

0148-0227/10/2010JF001747

Leopold and Wolman, 1960; *Keller*, 1971; *Lisle*, 1979; *Thompson et al.*, 1996, 1999; *Thompson and Hoffman*, 2001; *Milan et al.*, 2001; *Heritage and Milan*, 2004]. Alternate bars in straight reaches [*Mosley and Tindale*, 1985; *Lisle and Madej*, 1992; *Lisle and Hilton*, 1992; *Whiting*, 1996; *Lisle and Hilton*, 1999] and flumes [*Ikeda*, 1983; *Lisle et al.*, 1991, 1993] tend to have coarse bar tops and fine pools. In high-gradient streams, dynamic patches of fine material form in the wake zones of immobile accumulations of boulders or cobbles [*Garcia et al.*, 1999; *Laronne et al.*, 2000]. The size of these patches appears to be supply dependent, and sediment actively passes through them [*Yager*, 2006].

[4] The development of persistent sorting patterns and forced patches should depend on a number of controlling factors, such as stage-dependent flow fields, channel morphology, including bed topography and planform shape, local sediment supply, the grain size distribution of available sediment, and channel obstructions. However, we still lack a quantitative description of mechanistic processes that explicitly connect these variables, particularly for gravel bed channels where excess shear stress is low and the sediment is not fully mobile. *Parker and Klingeman* [1982] suggested that gravel beds are armored because equal mobility requires intrinsically less mobile coarse grains to be overrepresented on the bed surface. *Paola and Seal* [1995] proposed that in rivers that typically have spatially variable shear stress fields, bed patchiness arises in response to this spatial variability, creating equal mobility patches of different sizes that differentially pass finer sediment and lead to downstream fining. *Lisle and Hilton* [1999] attributed the coarse bars and fine pools they observed in their relatively straight study reaches to "downstream winnowing," where fine particles winnow out of coarse patches and are deposited somewhere downstream in a fine patch; this requires the coarse fraction to be at least temporarily immobile. Their observations of high shear stress in coarse zones and low stress in fine zones (at low flow) are consistent with this interpretation. Much of the riffle-pool literature [e.g., *Gilbert*, 1914; *Leopold and Wolman*, 1960; *Keller*, 1971; *Lisle*, 1979; *Thompson et al.*, 1996, 1999; *Thompson and Hoffman*, 2001; *Milan et al.*, 2001; *Heritage and Milan*, 2004; *Harrison and Keller*, 2007] suggests that in straight reaches with pools and riffles, a "velocity reversal," where the near bed velocity (and presumably, the boundary shear stress and sediment transport capacity) in the pool exceeds that of the riffle at high discharge but does not exceed it at low discharge, is responsible for the development of coarse riffles and fine pools. Building on this work, *MacWilliams et al.* [2006] suggested pool-riffle sequences are maintained through "flow convergence routing," in which the flow field downstream of a channel constriction converges in riffles at low flow and in pools at high flow, and *Sawyer et al.*'s [2010] field work indicated that this process occurs in large gravel bed rivers. *Lisle and Hilton* [1992] suggested that stage-dependent effects were responsible for pools filling with sand, the depth of which can serve as a proxy for sediment supply. While these studies have shed light on mechanisms important for the development of forced bed surface patches, none present simultaneous, detailed measurements of stage-dependent flow fields, bed load transport fields, and surface grain size patterns to fully support an explanatory hypothesis.

[5] Sediment supply has been shown to be a critical control on the surface structure of gravel bed rivers. *Dietrich et al.* [1989] suggested that armoring is largely a result of insufficient sediment supply, and *Nelson et al.*'s [2009] reanalysis of their data and new gravel-only data showed that reductions in sediment supply lead to an expansion of coarse fixed patches, and they found sediment supply to be a primary control on the dynamics and occurrence of free patches. *Lisle et al.* [1991, 1993] also observed that in a flume with bar topography, reducing the sediment supply led to changes in bed surface sorting and emergence of bars. *Kinerson*'s [1990] study of several field sites in northern California suggested that bed surface patchiness is correlated with sediment supply, and *Yarnell et al.*'s [2006] analysis of field and flume studies found that streams with intermediate relative sediment supply values exhibited the greatest habitat heterogeneity (corresponding to bed surface patchiness). *Buffington and Montgomery*'s [1999b] analysis of several flume studies found that the median grain size of the bed surface varied inversely with sediment supply. Hydraulic roughness elements like bank irregularities and large woody debris also can cause the bed surface to become finer than it otherwise would be in their absence [*Buffington and Montgomery*, 1999c].

[6] Planform geometry and cross-channel bed topography interact with the flow and sediment transport fields to produce bed sorting and forced patches. Early models for sorting in channel bends [*Kikkawa et al.*, 1976; *Bridge*, 1977; *Allen*, 1978] assumed that equilibrium channel conditions occur when the local cross-stream effect of particle weight is exactly balanced by drag from secondary circulations. Consequently, these models predict that particles will travel along lines of equal depth such that there is no net cross-stream transport, and the resulting bed surface will exhibit coarse particles in deep water where the inward component of shear stress is greatest and the outward slope is the highest, and the bed will be fine in shallow water where the inward shear and cross-stream slope are lowest. *Parker and Andrews* [1985] developed a model combining a simple representation of flow processes in a bend with the assumption that sorting is solely a result of the cross-streambed slope, arriving at an analytical solution that predicts coarse sediment follows a path from the inside bank to the outside bank of a bend apex. This model was later incorporated into computer simulations of channel migration [*Sun et al.*, 2001a, 2001b]. In contrast with earlier models, *Dietrich and Smith* [1984], *Dietrich* [1987], and *Dietrich and Whiting* [1989] built upon detailed field measurements of flow and sediment transport to develop a hypothesis that in fully mobile beds, equilibrium occurs when shear stress divergence is balanced by sediment transport divergence. Their observations indicated that shoaling of the flow over the point bar as the shear stress declines forces all sediment toward the pool, but counteracting secondary flows (and effects of currents along oblique dune fronts) preferentially transport finer sediment inward. Net transport of sediment toward the pool matches increasing boundary shear stress, but the finer sediment is shifted toward the inside bank due to differential transport by inward-directed secondary flows [*Parker and Andrews*, 1985; *Ikeda*, 1989; *Bridge*, 1992]. While these mechanisms have explained observations in sand-bedded channels, it is not clear

whether the same reasoning could be used to predict sorting in gravel bed rivers.

[7] It is tempting to hypothesize that channels locally maintain "threshold" conditions, in which the bed surface locally maintains a grain size distribution (or median grain size) that is just able to be mobilized during a characteristic flood. A standard parameter for grain mobilization is the Shields stress, τ^*,

$$\tau^* = \frac{\tau}{(\rho_s - \rho)gD}, \quad (1)$$

which attains a critical value τ_c^* at initial motion. Here τ is the boundary shear stress, ρ_s is the density of the sediment, ρ is the density of water, g is the gravitational constant, and D is the particle diameter. If threshold conditions are achieved and τ_c^* is a constant for all grain sizes, spatial variations in boundary shear stress would be linearly reflected in the surface grain size distribution [*Lisle et al.*, 2000]. This assumption is used to design channels [*Lane*, 1955] and can be used on a watershed scale to make predictions about what the reach-averaged median grain size would be in the absence of external roughness or sediment supply effects [e.g., *Power et al.*, 1998; *Buffington et al.*, 2004]. However, threshold conditions are unlikely to be the norm, as suggested by *Lisle et al.*'s [2000] study where, at several natural channels, they measured bed topography, mapped the surface grain size distribution, and modeled the bed shear stress at bankfull discharge, ultimately finding no correlation between local shear stress and bed grain size. Alternatively, *Dietrich* [1987] and *Dietrich and Whiting* [1989] argued that in gravel bedded meanders with low excess boundary shear stress and low sediment supply, shear stress divergences might be balanced by divergences in sediment transport achieved primarily though bed grain size adjustment rather than erosion or deposition. In this case bed surface patchiness develops to moderate local bed mobility such that the divergences of stress and sediment flux are in balance. The predictive capability of this hypothesis has yet to be verified due to a limited number of well-developed quantitative linkages between topographically controlled stress fields, the sediment transport field, and the bed surface grain size distribution.

[8] Here we attempt to improve our empirical understanding of these linkages using observations collected during a near field scale flume experiment. We use detailed measurements of the bed surface topography, grain size, and the flow and sediment transport fields over a gravel bed of quasi-steady alternate bars that produced persistent topography and forced patches. Our observations suggest that topographically forced boundary shear stress divergences are matched by size-selective sediment transport divergences. The resultant changes in local sediment supply are accommodated by local changes in bed surface grain size, forcing the development of patches that allow the maintenance of quasi-steady morphology.

2. Methods

[9] The observations presented in this paper were collected during a flume experiment conducted in the main channel at St. Anthony Falls Laboratory (SAFL) at the University of Minnesota in Minneapolis, MN. The experiment was part of the larger "StreamLab06" suite of experiments designed to examine the interactions between geomorphology, nutrient cycling, and biomass accumulation. The large scale of the flume enabled us to make local measurements of the bed surface, flow field, and sediment transport field over a bar sequence.

2.1. Flume Setup and Experimental Procedure

[10] The main channel at SAFL is a 2.75 m wide, 80 m long (with a 55 m long test section) rectangular cross-section concrete research channel that has recently been refurbished and reinstrumented. Initially, a homogeneous, flat bed was created by filling the flume with a gravel mixture composed of grains 2–45 mm in diameter with a median grain diameter of 11 mm (Figure 1a). Water discharge was held constant throughout the experiment at 400 ± 20 l/s.

[11] Sediment was recirculated throughout the experiment. Bed load exiting the flume was collected in five side-by-side sediment traps, which in total spanned the flume width. Each sediment trap was connected to a load cell, which sampled sediment discharge continuously in 1 s intervals. An impeller pump in the floor pit where the sediment traps were located would then return the sediment to the head of the flume (see *Marr et al.* [2010] for more information on the flume facilities and operation).

[12] Prior theoretical [*Blondeaux and Seminara*, 1985; *Colombini et al.*, 1987; *Lanzoni and Tubino*, 1999] and experimental [e.g., *Lanzoni*, 2000] work on alternate bars suggests that bar development requires a large width-to-depth ratio and full sediment mobility. *Wilcock and McArdell* [1993] suggested that in a sediment mixture of a grain size range similar to ours, full mobility of all grain sizes occurs when the Shields stress (equation (1)) is approximately twice the critical Shields number (assumed to equal 0.045). Considering these suggestions, we chose a design bed slope (0.013) and discharge (0.4 ± 0.02 m^3/s) that resulted in a width-to-depth ratio of 20 and a dimensionless shear stress ratio (τ^*/τ_c^*) of about 2 (see Table 1 for a summary of the hydraulic conditions during the experiment). Although most gravel bed rivers have slopes smaller than 0.013 [*Parker et al.*, 2007], the width of our flume necessitated a rather steep slope to simultaneously achieve the desired excess stress and large width-to-depth ratio necessary for bar formation. Details regarding the measurement of shear stress are presented in section 2.5. To further enhance the development of alternate bars, we constricted the flow at the flume entrance to 2/3 of the channel width, creating a flow perturbation at the inlet that allowed bars to form freely downstream.

[13] We ran the flume with constant discharge and sediment recirculation until the bed topography and bed load flux exiting the channel reached approximately steady state conditions. The water surface elevation was monitored using an ultrasonic water level sensor that traversed the flume on a mechanized cart that ran along rails above the flume walls. The water surface elevation was repeatedly measured along five longitudinal profiles spaced 500 mm apart in the cross-stream direction with the center transect located along the center of the flume. Measurements in the along-channel direction were obtained at 5 mm intervals. The mechanized cart was also equipped with an acoustic echo sounder that

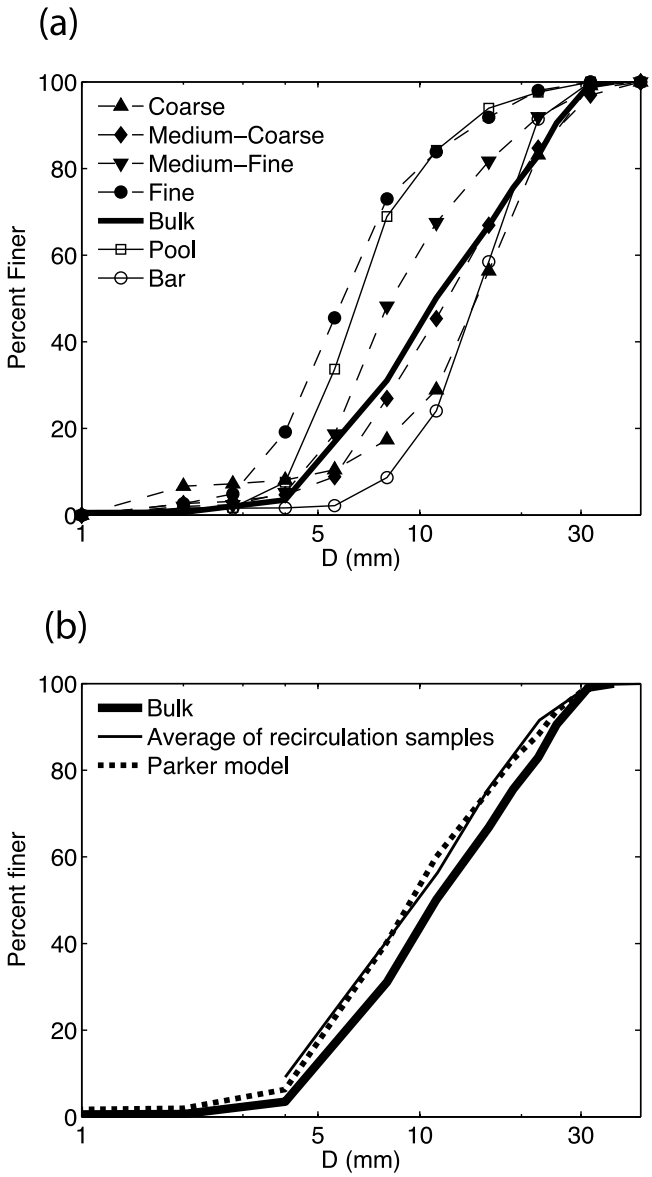

Figure 1. (a) Grain size distributions of the bulk sediment mixture, the four mapped patch types, and the bar and pool. (b) Grain size distributions for the bulk sediment mixture used to make the initial bed (thick line) and the average grain size distribution of the recirculation samples (thin line). The dashed line shows the grain size distribution of the bed load predicted by *Parker*'s [1990] bed load transport algorithm, using the flume-average shear stress (Table 1) and bulk sediment grain size distribution for the bed surface.

could measure bed surface elevation subaqueously; however, as bed topography developed, the flow became too shallow in some places for this instrument to function, so we relied upon dry bed topographic scans (described in section 2.3) to obtain bed surface elevation data.

2.2. Flow and Sediment Transport Measurements Over a Bar Sequence

[14] After the flume developed about a quasi-steady state topography consisting of about 1.5 alternate bar sequences, we made a series of local near-bed velocity, bed surface grain size, and sediment transport measurements over a bar sequence. We made measurements at 11 cross sections, spaced every three meters from $x = 14.5$ m to $x = 44.5$ m (we use x and y as downstream and cross-stream coordinates, respectively), with five points in each cross section spaced 50–60 cm apart (Figure 2a). At each point, we used a Pygmy current meter to measure the local velocity 3 cm above the bed. A Pygmy meter was chosen because initial attempts to measure the velocity with an acoustic Doppler anemometer (ADV) produced unreliable results. Velocity measurements were taken for an average of 55–60 s [*U.S. Bureau of Reclamation*, 2001]. Care was taken to ensure the Pygmy meter was oriented orthogonal to the flow, the direction of which was estimated visually with the aid of a string tied to the measurement rod. Although Pygmy meters generally are accurate to better than 3.5 per cent when used between about 6 and 30 cm above the bed, they may suffer from additional errors when placed closer to the bed [*Hubbard*, 1988]; therefore, in the following analysis we assume a 10 per cent uncertainty in measured near-bed velocity. After each velocity measurement, a photograph of the bed was taken with a digital camera placed in a waterproof housing that was attached to a pole. A scale bar was attached to the pole such that it typically appeared along the top of the underwater photographs, which generally covered an area of 7.1 cm by 5.3 cm. After the experiment, these photographs were analyzed in the lab to characterize the local bed grain size at the time of the velocity measurement. The b axis of each grain (as visible in the photographs, see *Bunte and Abt* [2001] or *Graham et al.* [2010] for a discussion of the possible effects of grain shape and imbrication on grain size distributions derived from photographs) was digitized by hand and the resulting area-by-number grain size distributions were converted to volume-by-weight distributions with the *Kellerhals and Bray* [1971] voidless cube model. Finally, in addition to the local velocity measurements and bed photographs, we measured the local bed load transport at each point on the grid by holding a miniature Helley-Smith-type of sediment sampler (similar to the traps used by *Dietrich and Smith* [1984]), which had a square opening with 5 cm sides and a nylon mesh bag attached to the downstream end to collect the sediment. The sampler was pointed directly upstream, and samples were taken for 60 s, although in some high-transport locations samples were shorter because the bag became filled with sediment. Each sediment sample was bagged, dried, and sieved. Although the bed surface topography appeared to be unchanging, we worked quickly and completed all of the local velocity and bed load transport measurements in under 5 h.

Table 1. Hydraulic Parameters

Parameter	Value
Discharge (m^3/s)	0.4 ± 0.02
Bed and water surface slope	0.013
Mean depth (cm)	13.5
Width/depth	20
Shear stress (Pa)	17.2
τ^*/τ_c^*	2

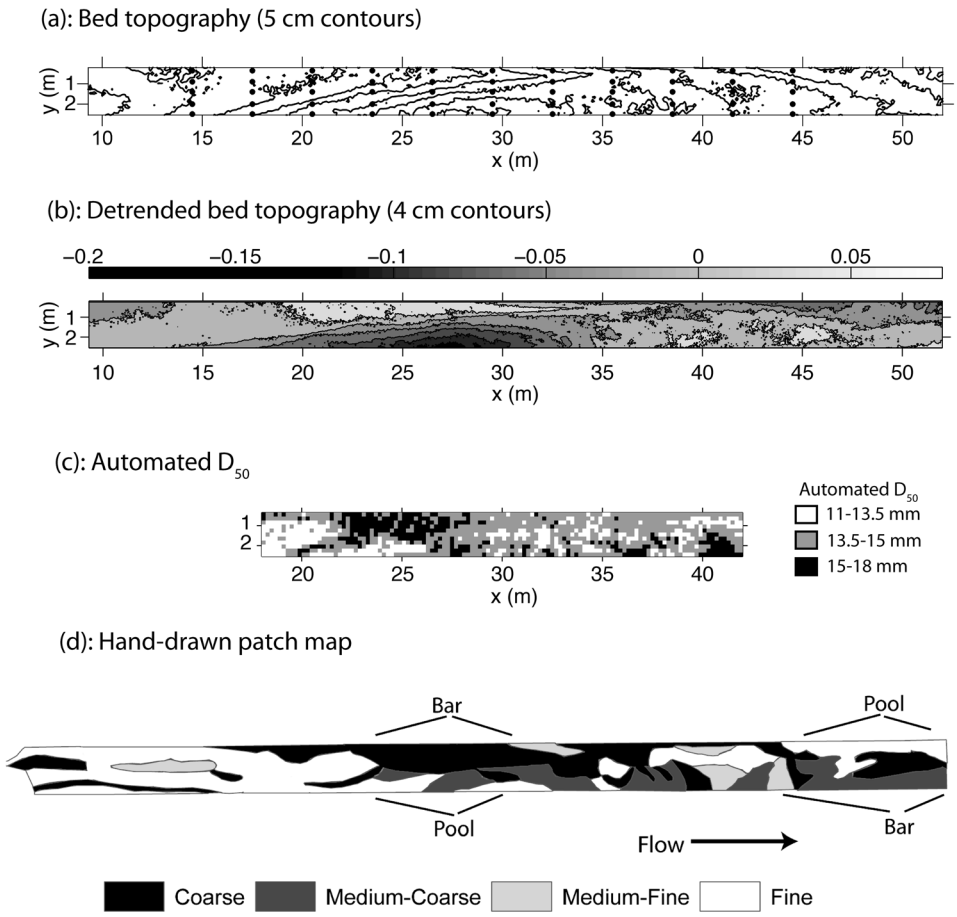

Figure 2. (a) Contour map of the quasi-equilibrium bed topography, generated from the 10 × 10 mm DEM. Flow is from left to right. The dots indicate the locations of velocity and bed load transport measurements at the 11 cross sections. (b) Contour map of the bed topography after subtracting the mean channel slope (S = 0.013); dark areas are low (pools) and light areas are high (bar tops). The grayscale bar intervals are shown in units of meters. (c) Map of the local median grain size D_{50} on a 20 × 20 cm grid, extracted from the 1 × 1 mm DEM using the automated grain size procedure; darker shading indicates a coarser surface. (d) Hand-drawn patch map. Approximate bar and pool locations are identified. The grain size distribution of each patch type is shown in Figure 1a. Each map has the same scale.

2.3. Bed Topography Measurements and Bed Surface Patchiness Characterization

[15] After all of the measurements taken while the flume was running were completed, the flume was rapidly drained, preserving the bed state as it existed at the end of the experiment. Bed surface patches were mapped by hand, wherein the bed was classified (by eye) into patches of similar grain size and sorting [e.g., *Nelson et al.*, 2009]. Four patch types were defined: fine (median grain size D_{50} of 5.9 mm, geometric standard deviation σ of 1.79), medium-fine (D_{50} = 8.3 mm, σ = 1.84), medium-coarse (D_{50} = 12.1 mm, σ = 1.92), and coarse (D_{50} = 14.7 mm, σ = 2.11). Figure 1a presents the volume-by-weight grain size distributions of these patch types. Eight bed surface samples were collected throughout the StreamLab06 experiments, in which 30 × 30 cm areas of the bed were painted and all painted particles were collected and sieved. *Kellerhals and Bray*'s [1971] method was then used to convert the area-by-weight grain size distributions to the volume-by-weight distributions commonly used in empirical bed load transport formulas. The painted areas were located so that they fell entirely within a particular patch on the hand-drawn map and so that all mapped facies types were represented by physical samples. The samples were averaged to obtain characteristic grain size distributions for each patch type.

[16] In addition to the patch maps, the quasi-equilibrium dry bed surface was characterized with a high-resolution 1 × 1 mm topographic scan generated by a range-finding laser attached to the motorized cart that traversed the bed. The 1 × 1 mm digital elevation model (DEM) covered a 24 m swath of the flume, from x = 18 m to x = 42 m. A coarser, 10 × 10 mm DEM was also generated, covering essentially the entire flume test section from x = 9 m to x = 55 m. A digital camera was also attached to the cart and a sequence of photographs of this larger region of the bed were taken.

2.4. Automated Bed Surface Grain Size Measurements

[17] We also characterized the spatial variability of the bed surface grain size distribution through an automated

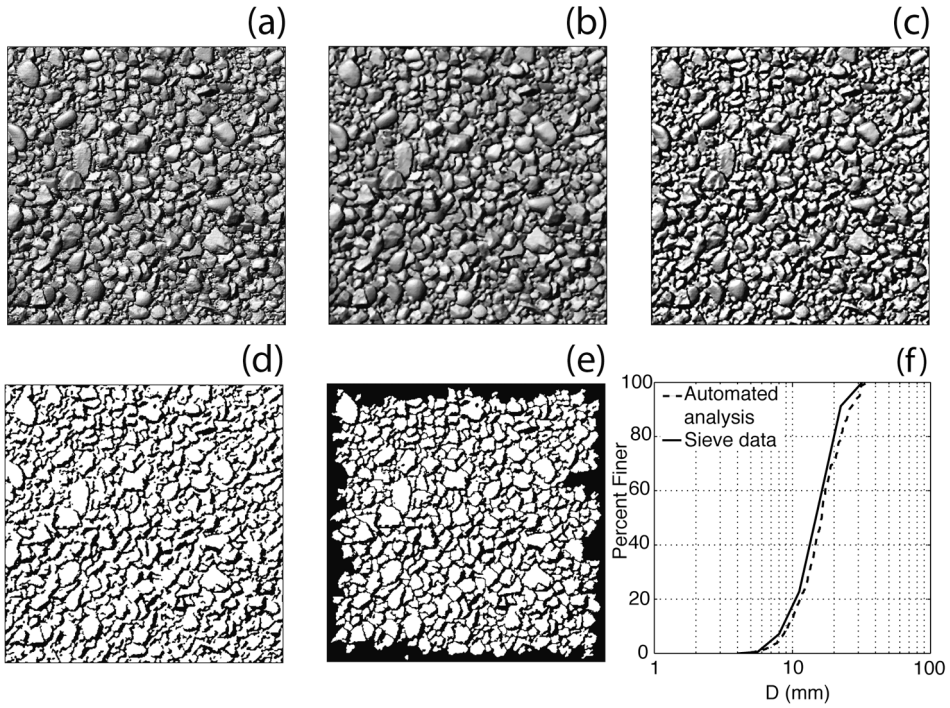

Figure 3. Example of steps performed in the automated image analysis, on a 30 × 30 cm square of the bed from which a surface sample was taken. (a) Original grayscale image of the 1 × 1 mm hill shade DEM; (b) image after application of a median filter; (c) image after the morphological bottom-hat filter is applied; (d) image after the double-thresholding procedure; (e) final segmented image, after application of the *h-minima* transform and the watershed algorithm; and (f) comparison of the volume-by-weight cumulative grain size distributions from the automated analysis and from sieving the surface sample.

image analysis procedure. Following the methodology of *Graham et al.* [2005a, 2005b], we used a shaded relief map generated from the 1 × 1 mm digital elevation model created from the high-resolution laser scan as an input image for automated grain extraction (similar to *McEwan et al.* [2000]). Although the resolution (on a pixels per millimeter basis) of the 1 × 1 mm DEM was not as high as the resolution of the bed photographs taken from the cart, we found the DEM provided more reliable results than the photographs; that is, the resultant grain size distributions better matched those from surface samples, because the DEM image displayed stronger contrast between grains, the variability within grains due to lithology was eliminated, spatial registration was exact, and there were no perspective issues to correct. Grain size statistics for the portion of the flume covered by the 1 × 1 mm DEM were calculated on a 20 × 20 cm grid in the following manner: A 30 × 30 cm window was centered at each grid point and the hill shade image was cropped to that window size. *Graham et al.*'s [2005a] method was then applied to the 30 × 30 cm neighborhood and the local D_{50} was calculated from its output. While the reader should refer to *Graham et al.* [2005a] for a complete description of their method, a summary of the technique and the parameters we used is described below.

[18] *Graham et al.*'s [2005a] method essentially uses pixel intensity to delineate individual sediment grains. It does this by dividing the image into regions, where each region represents a single grain. Because grain boundaries tend to be darker than the grains themselves, the method uses the intensity to detect grain edges. Initially, a median filter is applied to the image (in our case, the 30 × 30 cm crop of the hill shade DEM) to help blur out image noise and grain imperfections. A morphological bottom-hat filter using a disk structuring element is then applied to the image to enhance the contrast. A double-threshold method is then used to determine which pixels are likely grain edges. Here two threshold intensities are selected; one threshold corresponding to very dark pixels (which almost certainly are grain edges) and a second, lower threshold corresponding to somewhat dark pixels that are potentially grain edges. Features in the lower threshold image that overlap those in the higher threshold image are then classified as edges. The resulting binary image is then divided into regions using the watershed segmentation algorithm [*Vincent and Soille*, 1991]. Because the watershed segmentation can often produce oversegmented images, *Graham et al.* [2005a] perform an *h-minima* transform to suppress small pits prior to the application of the watershed algorithm. Figure 3 shows an example portion of our hill shade DEM at various stages in the grain identification process.

[19] Once the grains have been identified as regions, an ellipse is fit to each region and the minor axis of the ellipse

Table 2. Parameters Used in the Automated Grain Size Analysis

Parameter	Value
Median filter size	3 pixels
Structuring element disk radius	5 pixels
Low threshold	1%
High threshold	35%
h-minima threshold	1 pixel

is measured (in pixels). *Graham et al.* [2005a] found this technique gives a reasonably accurate estimate of the true *b* axis of each grain. The resulting list of grain diameters is then converted to mm using the known image scale (in our case, 1 pixel = 1 mm), and grain size distributions are generated. Importantly, the grain size distributions must be concatenated at an appropriate level to avoid spurious measurement of image noise [*Graham et al.*, 2005a, 2005b, 2005c]. We concatenated our grain estimated grain size distributions at 4 mm because our experiment involved only gravel and since visual observation (and comparison with surface samples) suggested that the automated results were reasonable to that level.

[20] We found that the *h-minima* transform had positive or negative consequences on the accuracy of the algorithm depending on the type of surface being analyzed. Without the *h-minima* transform, coarse surfaces (such as the one displayed in Figure 3a) would be oversegmented by the watershed algorithm, and inclusion of a 1 pixel *h-minima* transform improved the accuracy considerably (e.g., Figure 3f). However, finer bed surfaces were better characterized without the *h-minima* transform, since the watershed algorithm tended not to oversegment in these cases. While the importance of the *h-minima* transform is likely related to the 1 mm/pixel scale of our DEM, it does mean that the use of a single *h-minima* parameter for analysis of the entire DEM will produce either too fine distributions for coarse areas (if *h-minima* = 0) or too coarse distributions for fine areas (if *h-minima* = 1). Nevertheless, the overall pattern of sorting is essentially the same either way, so for the remainder of this paper, grain size data generated from the automated procedure are presented with *h-minima* = 1. Table 2 shows the parameters we used in the image analysis algorithm.

2.5. Shear Stress Calculations

[21] Local boundary shear stress was estimated in two ways. First we used the single velocity method described by *Dietrich and Whiting* [1989], in which shear stress is estimated from a single measurement of the near bed velocity. The law of the wall describes the vertical profile of downstream velocity near the boundary:

$$u(z) = \frac{u_*}{\kappa} \ln\left(\frac{z}{z_0}\right), \tag{2}$$

where $u(z)$ is the velocity at height z above the bed, z_0 is the roughness height, κ is von Karman's constant ($\kappa = 0.4$), and u_* is the shear velocity, which is defined as

$$u_* \equiv \sqrt{\tau/\rho}. \tag{3}$$

Here τ is the boundary shear stress and ρ is the fluid density. Using the law of the wall, the boundary shear stress can be estimated from a single velocity measurement $u(z)$ as

$$\tau = \rho \left[\frac{u(z)\kappa}{\ln(z/z_0)}\right]^2. \tag{4}$$

The roughness height, z_0, is commonly parameterized to scale with the coarse grains on the bed; for instance:

$$z_0 = AD_{84}. \tag{5}$$

Here D_{84} is the grain size for which 84% of the grains on the bed surface are finer. Following *Leopold and Wolman* [1957], *Dietrich and Whiting* [1989] suggested $A = 0.1$ is a reasonable scaling factor, which we use here. *Wilcock* [1996] found that the single velocity method for estimating u_* was accurate to within about 7%, using a roughness height of $z_0 = 0.095D_{90}$, which is essentially equal to $z_0 = 0.1D_{84}$ used here and $z_0 = 0.09D_{84}$, found by *Wiberg and Smith* [1991]. Using this formulation, we estimated the local shear stress on our grid of velocity measurements using the measured velocity at $z = 3$ cm above the bed, with a D_{84} estimated from the grain size distributions derived from the underwater photographs.

[22] Despite its simplicity, the single-velocity method has been shown to produce more reasonable and reliable estimates of boundary shear stress than other more complicated techniques. *Whiting and Dietrich* [1990] found that the single-velocity method outperformed a method using the slope of the velocity profile because the latter method projected well into the flow and included large-scale drag, causing the boundary shear stress to be overestimated. They also pointed out that the near-bed velocity measurement can avoid upstream influences of features such as dunes or bank irregularities, suggesting that instead this method captures primarily the effects of local grain roughness essential to sediment transport. The usefulness of incorporating the local grain size into stress calculations has more recently been confirmed by *Sime et al.* [2007], who found that an unconstrained velocity gradient estimate of shear stress leads to greater error than a grain size constrained profile. The single-velocity method relies upon the assumption of a logarithmic near-bed velocity profile, which may not occur in areas of high relative roughness ($h/D_{84} > \sim 5$) [*Wiberg and Smith*, 1991; *Bathurst*, 2002; *Katul et al.*, 2002]. Since our flume developed shallow flow over coarse bar tops, the velocity profile there may differ from logarithmic and thus the single-velocity method may overestimate or underestimate the local boundary shear stress, but in the absence of velocity profiles over the bar top we proceed with the assumption of a logarithmic profile.

[23] The discrete spacing of velocity measurements, and the lack of data on velocity (and boundary shear stress) direction, suggests that an additional method of modeling the entire boundary shear stress field, constrained by measurements, is in order. We used a quasi-three-dimensional hydrodynamic model, FaSTMECH (Flow and Sediment Transport and Morphological Evolution of Channels, available online at http://wwwbrr.cr.usgs.gov/gstl/project-MDSWMS.html), which was developed by the U.S. Geological Survey and has been described in a number of

studies [e.g., *Lisle et al.*, 2000; *Kinzel et al.*, 2009]. For a full description of the model, the reader is directed to the work by *Nelson and McDonald* [1995] and the USGS online documentation, but, in summary, the model solves the full vertically averaged and Reynolds-averaged momentum equations and it incorporates a vertical structure submodel that computes the vertical velocity profile along the streamlines of the vertically averaged flow and the secondary flow across those streamlines. The vertically averaged equations are cast in a channel-fitted coordinate system and are derived and presented by *Nelson and Smith* [1989]. In its computation of the depth-averaged solution, the model assumes steady, hydrostatic flow and models turbulence with an isotropic eddy viscosity. The vertical submodel takes the solution to the depth-averaged model and an assumed eddy viscosity structure [*Rattray and Mitsuda*, 1974] to calculate the three-dimensional solution. While a fully three-dimensional model might be capable of calculating more reliable estimates of boundary shear stress than a two-dimensional model like FaSTMECH, three-dimensional models inherently require detailed measurements of the three-dimensional flow field for calibration and are highly sensitive to the method of specifying topographic complexity [*Lane et al.*, 1999]. Given the difficulty we encountered in measuring the 3-D velocity field with an ADV (Section 2.2), the 2-D modeling capabilities of FaSTMECH are appropriate for this exercise.

[24] The momentum equations are solved over a curvilinear orthogonal finite difference grid, constructed in the graphical user interface MD_SWMS (Multidimensional Surface Water Modeling System) with which FaSTMECH is distributed [*McDonald et al.*, 2005]. The Cartesian grid we used to model the SAFL flume had 8 cm node spacing in both the x and y directions. Elevation data from the 10 × 10 mm DEM were interpolated onto the grid points.

[25] We provided the model a constant discharge upstream boundary condition of 0.4 m^3/s, and we specified a constant downstream water surface elevation and a constant lateral eddy viscosity of 0.0019 m^2/s. We used spatially variable roughness in which the drag coefficient C_d was estimated to be a function of the flow depth computed from constant roughness conditions and the local D_{84} estimated from the automated image analysis [e.g., *Nelson et al.*, 2003]. We calibrated the roughness by matching the model-predicted water surface elevation to the five longitudinal water surface profiles collected by the ultrasonic water level sensor during the experiment, and by comparing the model-predicted flow velocity 3 cm above the bed to the pygmy meter velocity measurements; the C_d parameter ranged from 0.0034 to 0.0142. The calculated shear stress field was similar to one calculated with a constant roughness with $C_d = 0.009$, but the variable roughness solution did a better job matching our near-bed velocity measurements. After calibration, the root-mean-square error in our calculated water surface elevation was 0.0146 m and the root-mean-square error between the calculated and measured near-bed velocities was 0.11 m/s. The model's convergence (the per cent deviation between the predicted discharge at a grid cross section and the specified discharge) was between ±0.07 per cent.

[26] The single-velocity method provides a useful check on the FaSTMECH output. However, because the model provides a continuous estimate of the entire stress field, including the magnitude and direction of the local stress vectors, we focus on and use those estimates throughout our subsequent analysis.

3. Observations

3.1. Bed Surface Topography and Sorting

[27] Alternate bars began to form shortly after the experiment began and they immediately started to migrate downstream; however, their rate of migration slowed as the bar amplitude became more pronounced and after about 13 h the bars appeared visually to have stopped migrating. Repeat scans of the water surface indicated that there was little to no change in the water surface (Figure 4b), which corroborated the visual observations that a quasi-steady state condition had developed.

[28] The establishment of quasi-steady conditions was further verified through analysis of the sediment flux exiting the downstream end of the flume (Figure 4a). For 15 h leading up to the bed load and velocity measurements and the 5 h during which the measurements were taken, the total bed load flux collected in the downstream weigh pans generally ranged from about 0.5 to 2.5 kg/s with occasional deviations from 0.0 to 3.0 kg/s (Figure 4a). In spite of this variability, which is an inherent feature of sediment transport [e.g., *Pitlick*, 1988; *Nelson et al.*, 2009; *Singh et al.*, 2009], a linear regression of the time series has a slope of 10^{-5} kg/s/h, indicating that quasi-steady conditions persisted throughout this period. The four sediment recirculation samples taken during this time (Figure 4a) had very similar grain size distributions, the average of which is presented in Figure 1b. All grain sizes from the bulk sample were present in the recirculation samples. Interestingly, if *Parker*'s [1990] surface-based bed load transport algorithm is provided with the flume-averaged boundary shear stress ($\tau = 17.2$ Pa) and the bulk sediment grain size distribution to characterize the surface, the algorithm calculates a bed load grain size distribution virtually identical to our averaged recirculation samples (Figure 1b), suggesting that *Parker*'s [1990] algorithm is well suited for modeling our experiment.

[29] The quasi-steady state bed developed about 1.5 complete bar-pool sequences. Bar heads were located at approximately $x = 11$ m, $x = 35$ m, and $x = 55$ m (Figures 2a and 2b), indicating a bar wavelength of about 44 m. The furthest upstream bar's location was forced by the placement of sandbags at the flume entrance, and the furthest downstream bar was almost completely developed before reaching the flume outlet. The bar tops were about 25 cm higher than the adjacent pools (Figure 2a). By the time we began to make velocity and sediment transport measurements, the bed configuration was essentially unchanging.

[30] In general, the bed surface on bar tops was coarse, and the bed surface in pools was fine (Figures 2c and 2d). Surface samples of the bar top and pool (Figure 1a) indicate that the D_{50} of the bar top was 14.6 mm and the D_{50} of the pool was 6.6 mm. The hand-drawn patch map (Figure 2d) shows that while there is some local variability in grain size pattern, this general pattern of coarse bars and fine pools predominated in our system.

[31] The map of median grain size generated from the automated image analysis (Figure 2c) shows essentially the same pattern as the hand-drawn patch map. This internal consistency is encouraging as it suggests that both methods

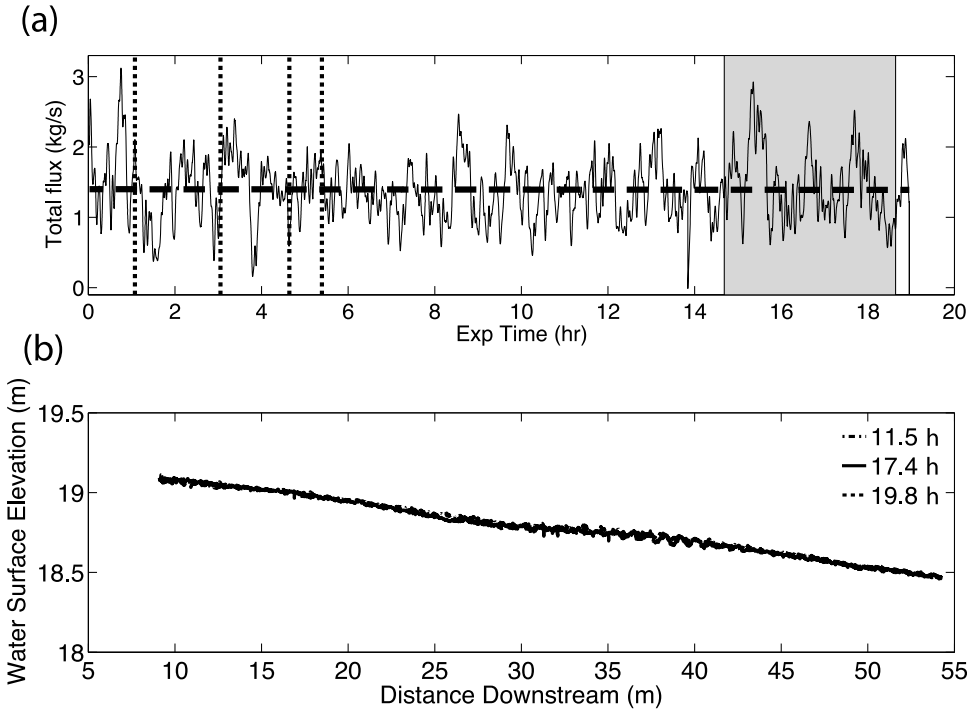

Figure 4. (a) Time series of total sediment flux exiting the flume captured by the weigh pans. The dashed horizontal line is a best fit linear regression to the time series data (slope $\approx 10^{-5}$ kg/s/h), the four vertical dashed lines indicate collection times for sediment recirculation samples in Figure 1b, and the shaded gray region represents the period over which bed load and velocity measurements were taken. (b) Three water surface scans taken along the channel centerline before and after velocity and bed load transport measurements were started. The time of each profile, corresponding to the horizontal axis in Figure 4a, is shown in the legend. The substantial overlap of the profiles, along with visual observations of the bed, suggests quasi-steady state conditions.

are effectively capturing the overall sorting structure that developed on the bed. The estimated D_{50} of the bar tops from the automated procedure is generally around 14–18 mm, which is consistent with the sieved surface sample. The automated procedure overestimates the D_{50} of the pools to be around 11–13 mm, probably due to the inclusion of the *h-minima* threshold everywhere (as discussed in section 2.4). Table 3 shows the number of cells from each class of the automated image analysis that are co-located in each class of the hand-drawn patch map, indicating that in general there is good agreement between the two methods. The overall pattern of coarse bars and fine pools prevails regardless of the method used to assess it.

[32] The sorting maps in Figures 2c and 2d are useful for visualizing the overall sorting patterns on the flume bed, but in reality the transition from one patch to another may not be as sharp as the boundaries on the maps suggest. Figure 5a illustrates in detail how the automated image analysis map and the 1 × 1 mm DEM compare with each other. In general, a visual assessment shows that areas of the bed that are obviously coarse or fine are placed in the appropriate patch category, although the precise location of the boundary depends upon the details of the classification method (in this case, the value of the automated D_{50} at the transition between classes). So the discrete boundaries in Figures 2c and 2d might more accurately be thought of as fuzzy boundaries rather than sharp transitions from one patch to another. Research into more sophisticated characterization of objective bed surface patch delineation is ongoing.

3.2. Flow Field

[33] The model-predicted stress field is spatially heterogeneous (Figure 6a). The zone of maximum shear stress shifts from the left side of the channel (looking downstream) at the upstream end of the flume toward the right side of the flume by about x = 25 m. The large bar on the left side of the channel between x = 20 and x = 35 m directs most of the flow to the right, producing reach-maximum calculated stresses of around 30 Pa in the adjacent pool. Downstream of that bar, the developing bar on the right side of the channel directs flow, and the zone of maximum shear stress, toward the left wall. The oscillations visible in the stress map in Figure 6a are not numerical instabilities; they appear instead to be a result of small-scale bed forms present in the scanned topography used to create the computational mesh.

Table 3. Number of Cells From the Automated Grain Size Analysis (Figure 2c) Located in Each Patch Class on the Hand-Drawn Patch Map (Figure 2d)

Automated D_{50} (mm)	Coarse	Medium-Coarse	Medium-Fine	Fine
15–18	215	58	13	19
13.5–15	359	149	62	161
11–13.5	65	79	16	230

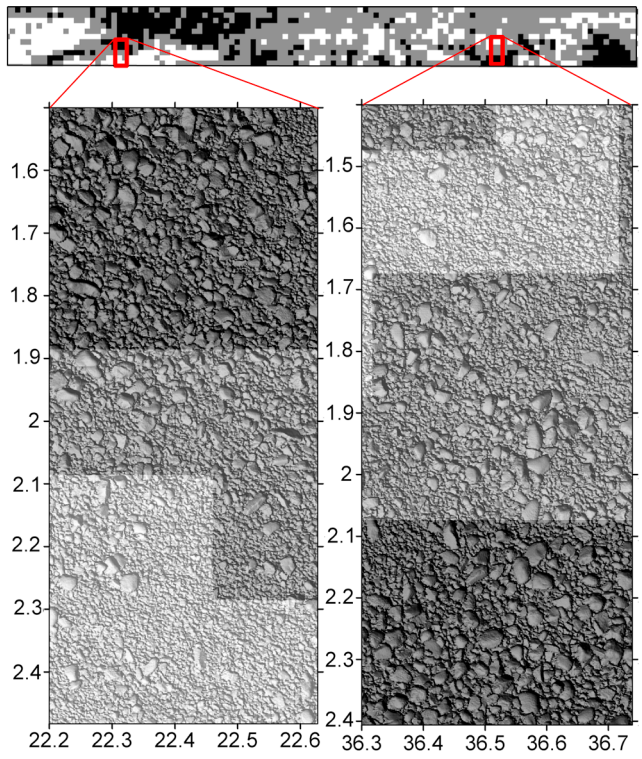

Figure 5. Results from the automated image analysis (Figure 2c) overlain on portions of the 1 × 1 mm DEM. Numbers along the axes indicate cross-stream and downstream position in meters.

Although the water was too turbid to make direct bed surface observations during the experiment, according to the unified bed form phase diagram presented by *Best* [1996], dunes or bed load sheets can be expected for our hydraulic conditions and sediment mixture.

[34] Figure 7a compares the model-predicted water surface elevation with the observed profiles for the three middle longitudinal profiles. There is excellent agreement, except at about x = 31 m where the echo sounder measured a small (probably transient) wave that was not calculated by the steady state model. Figures 7b–7e show comparisons between the velocity measured 3 cm above the bed with the pygmy meter and the near-bed velocity computed with FaSTMECH's vertical profile submodel, as well as comparisons between the boundary shear stress calculated with the single velocity measurements and the FaSTMECH-computed boundary shear stress. The error bars on the velocity measurements represent 10% uncertainty, and those on the single-velocity stress measurements are estimated through Gaussian error propagation assuming 10% uncertainty in the measured velocity $u(z)$, 30% uncertainty in the D_{84} estimated from the underwater photographs, and uncertainties of 5 mm for z and 0.02 for A. The agreement in near-bed velocity is generally quite good, and in general there is reasonable agreement between the two methods of computing boundary shear stress despite the uncertainty in many of the parameters used in the single-velocity calculation (equation (4)). Because boundary shear stress is modeled as a function of the square of the depth-averaged velocity [*Nelson et al.*, 2003], one should expect it to be more difficult for the model to match stress estimates than velocities.

3.3. Sediment Transport Field

[35] Table 4 presents the total downstream flux Q_s for each section, which were computed from the five measurements taken across each section as $Q_s = \int_{-W/2}^{W/2} q_s dy$, where W is the width of the channel and y is the cross-stream coordinate. The mean value of the measurements, 1258 g/s, is close to the average sediment flux exiting the flume of about 1400 g/s (Figure 4a).

[36] There was substantial cross-stream variation in the downstream-oriented sediment transport we measured. Figure 6a presents cross-sectional profiles of the downstream sediment transport q_s. To facilitate comparison between cross sections (using a method previously adopted in other studies [e.g., *Dietrich and Smith*, 1984]), the data have been corrected such that the total downstream transport at each section equals the mean value of 1258 g/s from Table 4. The coefficient of variation (standard deviation/mean) of these measurements was 0.22, which, considering the brief duration of measurements and considerable cross-stream variability, we think makes such a correction reasonable for purposes of comparison (*Dietrich and Smith* [1984] observed a coefficient of variation of 0.25 in the downstream sediment flux in their field study of Muddy Creek). Downstream sediment transport tended to follow the zone of maximum shear stress (Figure 6a), with the highest measured values in the high-stress pools. Although the bed load measurements were sieved, we present only the total flux data since it is unlikely our samples were large enough to get accurate grain size distributions of the bed load [e.g., *Dietrich and Whiting*, 1989].

[37] Sediment was not moving solely in the downstream direction. Because we oriented our bed load samplers directly upstream, thereby sampling only the downstream component of the local sediment flux q_s, we can calculate the local cross-stream sediment flux q_n if we take advantage of a steady state assumption. The generalized grain size specific two-dimensional conservation of bed sediment equation can be written as [*Parker*, 2008]

$$(1-\lambda_p)\left[f_{li}\frac{\partial \eta}{\partial t}+\frac{\partial}{\partial t}(L_a F_i)\right] = -\frac{\partial q_{i,s}}{\partial s}-\frac{\partial q_{i,n}}{\partial n}, \qquad (6)$$

where λ_p is the bed porosity, η is the bed elevation, t is time, f_{li} is the fraction of the ith grain size transferred between the surface and the subsurface during aggradation or degradation, L_a is the active layer thickness [e.g., *Hirano*, 1971], F_i is the fraction of the ith grain size on the bed surface, and $q_{i,s}$ and $q_{i,n}$ are the volume bed load transport rates per unit width of the ith grain size in the downstream (s) and cross-stream (n) directions. Following the right-hand rule, we consider the s coordinate to be positive in the downstream direction and the n coordinate to be positive toward the left bank. If we assume steady state conditions, the time derivatives in equation (6) go to zero and we arrive at a rela-

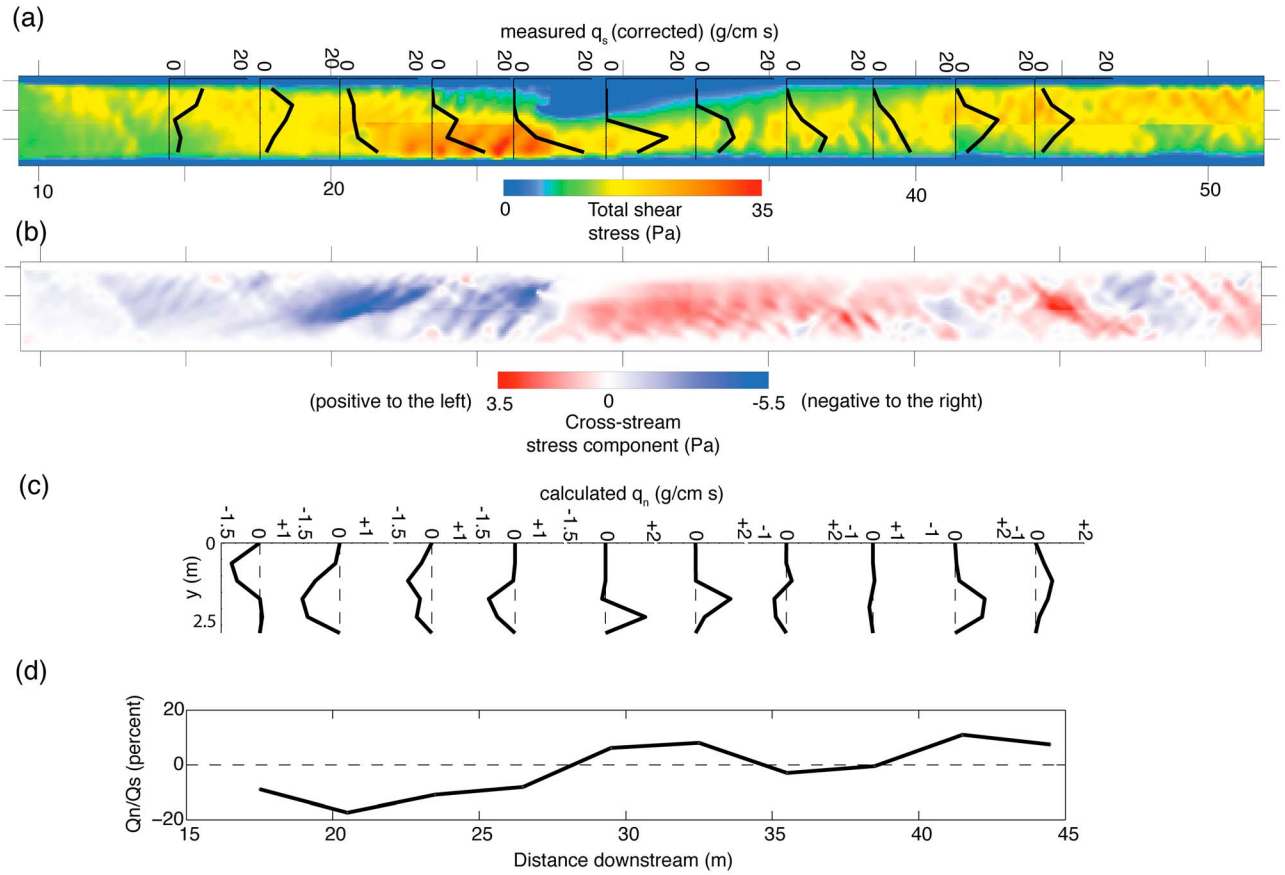

Figure 6. Shear stress and sediment transport measurements and estimates. (a) The color map is the total boundary shear stress computed in FaSTMECH. Overlain on the map are plots of measured downstream sediment flux per unit width, q_s, the magnitudes of which have been corrected such that the total downstream flux at each cross section equals the mean across all sections (see text). (b) A map of the cross-stream component of the boundary shear stress computed by FaSTMECH. (c) Cross-stream sediment flux rates (q_n) computed from the q_s data in Figure 6a and equation (8). Positive q_n values are toward the left bank. (d) Ratio of the total cross-stream sediment flux to total downstream sediment flux at each cross section. Again, positive values are toward the left bank. Note that the x axes of all plots are aligned for easy comparison, and that Figures 6a and 6b cover the same area as the contour map in Figure 2. Flow is from left to right.

tionship between the downstream and cross stream fractional transport rates:

$$\frac{\partial q_{i,n}}{\partial n} = -\frac{\partial q_{i,s}}{\partial s}. \tag{7}$$

This equation can be integrated to solve for the cross-stream sediment flux:

$$q_{i,n} = -\int_{-W/2}^{n} \frac{\partial q_{i,s}}{\partial s} dn. \tag{8}$$

We used equation (8) with our measured downstream bed load transport rates $q_{i,s}$ (corrected to integrate to the mean total flux at each cross section) to calculate the cross-stream bed load transport rates $q_{i,n}$ necessary for steady state. Doing so requires the additional boundary condition of zero flux at the flume walls: $q_{i,n} = 0$ at $n = -W/2$ and $W/2$. We evaluated $\partial q_{i,s}/\partial s$ with a forward difference calculation, so the first cross section for which we were able to calculate cross-stream flux was cross section 2 at x = 17.5 m. Note that in our experiment, the (s, n) coordinates can be replaced with (x, y) because we are working in a straight flume.

[38] The calculated cross-stream sediment fluxes (summed over all grain sizes) are presented in Figure 6c. In the upstream portion of the flume, where there is a prominent bar on the left side of the channel (facing downstream), cross stream transport is primarily to the right. Going downstream, as the bar is passed (and another bar begins to form on the right side of the channel), at around x = 28 m, the cross-stream sediment flux changes direction and becomes primarily oriented toward the left bank. This is more readily illustrated in Figure 6d, where we have plotted the ratio of the integrated cross-stream flux Q_n ($Q_n = \int_{-W/2}^{W/2} q_n dn$) to the integrated downstream flux Q_s (which, because we are using the corrected data, is the mean value for each section) as a function of distance downstream. In the upstream portion of the channel, there is net transport to the right, and downstream of the bar there is net transport to the left. The

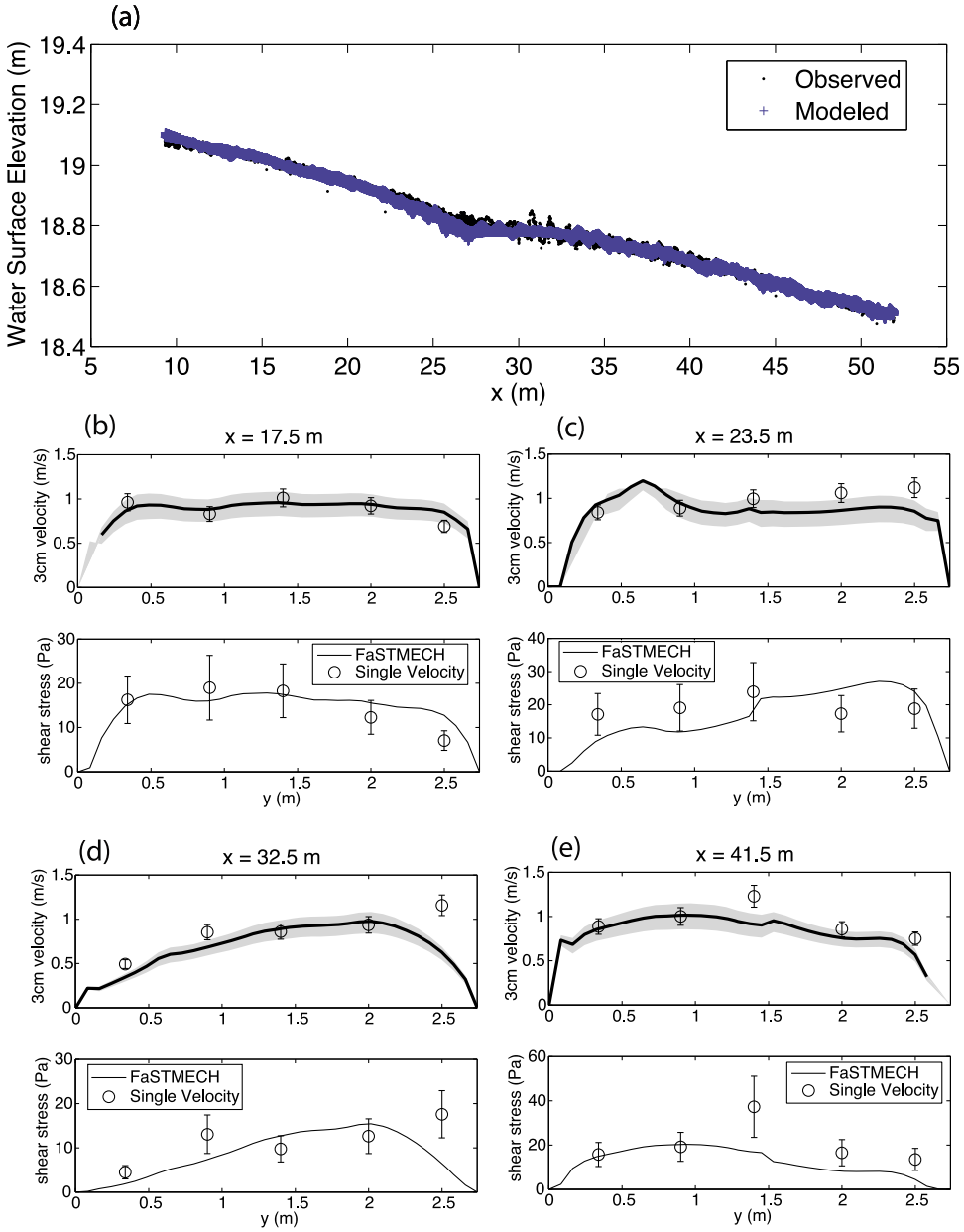

Figure 7. (a) Measured and model-predicted water surface elevation in the downstream direction for the three middle longitudinal profiles measured with the echo sounder (y = 0.87 m, y = 1.37 m, and y = 1.87 m). (b–e) Comparisons of measured and model-predicted velocity and boundary shear stress for four cross sections. In the velocity plots (Figures 7b (top)–7e (top)), the measured velocities are from 3 cm above the bed surface; the shaded region is the model-predicted velocity between 2 and 4 cm above the bed, and the solid line is the model-predicted velocity at 3 cm above the bed. Figures 7b (bottom)–7e (bottom) show boundary shear stress estimated from the single-velocity method (equation (4)) and calculated by FaSTMECH.

magnitude of the Q_n/Q_s ratio is ±18%, which is in the range of *Dietrich and Smith*'s [1984] observations at Muddy Creek.

[39] This change in direction of net cross stream transport coincides nicely with the cross-stream component of shear stress predicted by the FaSTMECH model (Figure 6b). The model predicts shear stresses oriented to the right in the upstream portion of the channel, changing direction toward the left downstream of x = 28 m. The internal consistency between our measured and computed sediment transport rates and the computed shear stress field is an encouraging sign that our observations and modeling are capturing the essential dynamics of our system.

4. Discussion

[40] Our flume observations provide an opportunity to examine how topography and the flow and sediment trans-

Table 4. Total Downstream Sediment Flux Measured at Each Cross Section ($\int_{-W/2}^{W/2} q_s dy$)

Cross Section	x Coordinate (m)	Total Downstream Sediment Flux (g/s)
1	14.5	1284
2	17.5	1777
3	20.5	818
4	23.5	1323
5	26.5	1226
6	29.5	1041
7	32.5	1294
8	35.5	1457
9	38.5	1573
10	41.5	1082
11	44.5	967
Mean		1258
Standard deviation		278
Coefficient of variation		0.22

port fields interact to produce forced patches and persistent sorting. Our observations do not suggest that our flume experiment demonstrated "threshold" conditions; like *Lisle et al.* [2000], we did not find a simple correlation between the local median bed surface grain size and the local shear stress. Instead, our results show that in places the shear stress and grain size appear to be positively correlated (both stress and grain size increasing or decreasing), negatively correlated (stress increasing while grain size decreases, or vice versa), or insignificantly correlated. We propose that this is a direct consequence of the particular dynamics of the size-selective nature of mixed-grain size gravel transport interacting with topographically induced steering of the flow [e.g., *Clayton and Pitlick*, 2007].

[41] Figure 8 shows FaSTMECH-calculated shear stress and surface D_{50} estimates from the automated grain size analysis along a profile at position y = 0.8 m from the left bank (Figure 2a). Most of this profile is in an area of the bed classified in the coarser (darker) facies on the hand-drawn patch map (Figure 2d), and since the *h-minima* = 1 parameter worked well in the coarser areas of the bed (Figure 3f), the D_{50} values presented in Figure 8 should be reasonable estimates of the magnitude of the actual surface D_{50}. Since much of the transect falls in the same patch type, the variation in D_{50} illustrated by the automated analysis, which can have a significant impact on local sediment transport rates, evidently was not detectable by eye. Along the y = 0.8 m profile, between x = 18 m and x = 23 m the boundary shear stress is essentially constant whereas the median grain size increases. Then from x = 23 m to x = 29 m the boundary shear stress drops dramatically and the grain size declines. From x = 29 m to x = 41 m the boundary shear stress increases, but the grain size progressively declines.

[42] An important piece missing from Figure 8 is the cross-stream component of the sediment transport field, which covaries with the boundary shear stress field and the surface grain size such that quasi-steady topography and sorting patterns are produced. In their description of fixed bars that developed in a high-gradient flume, *Lisle et al.* [1991] suggested that their stationary bars formed due to deposition of coarse material at the front of the bar preventing bar erosion and causing flow and sediment transport to be directed around the bar due to shoaling and "topographic steering" [e.g., *Dietrich and Smith*, 1984; *Smith and McLean*, 1984; *Nelson and Smith*, 1989]. Figure 6 shows that, in our flume, cross-stream bed load transport away from zones of decreasing boundary shear stress and toward zones of increasing shear stress occurred and this could lead to a dynamically stable bed topography and surface grain size distribution.

[43] Figure 9 places the observations of Figure 8 in the context of stress-grain size-transport rate relationships built into *Parker*'s [1990] surface-based bed load transport model. The procedure used to make the contours of total bed load flux in Figure 8 is similar to that presented by *Nelson et al.* [2009], in which we compute the total bed load transport rate predicted by the algorithm as a function of boundary shear stress and surface geometric mean grain size for synthetic bed surface distributions that have a wide range of mean grain sizes but constant geometric standard deviation (here, σ = 1.7, close to the bulk standard deviation of 1.8). The use of thousands of synthetic grain size distributions in this analysis allows us to fully explore the effects of changes in grain size statistics on predicted sediment transport rates. Also shown on Figure 8 are the shear stress (from FaSTMECH) and observed bed surface geometric mean grain size (from the automated image analysis) for four locations along the y = 0.8 m transect shown in Figure 8, which when connected show the path the transect followed in stress-grain size-flux space. Between x = 18 m to x = 23 m,

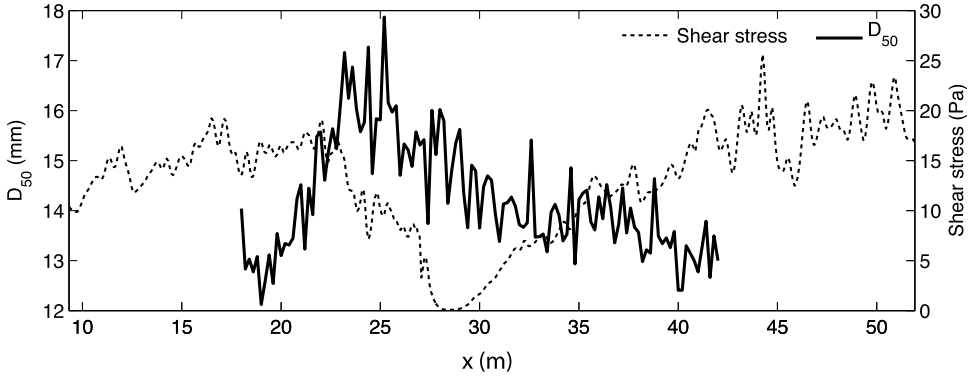

Figure 8. Longitudinal profiles of FaSTMECH-computed boundary shear stress (from Figure 6a) and bed surface D_{50} generated from the automated image analysis (from Figure 2c) along a transect of y = 0.8 m.

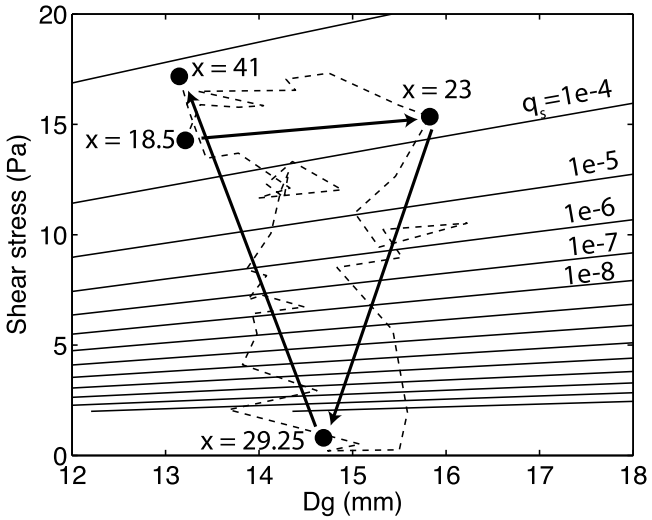

Figure 9. Contours illustrating the relationship between the total bed load transport rate, predicted by *Parker*'s [1990] model, boundary shear stress, and bed surface grain size. Here D_g is the geometric mean of the bed surface grain size distribution, and the standard deviation of the bed surface grain size distribution is held constant at σ = 1.7. Each contour line represents an order of magnitude change in transport rate (in m^2/s). Also shown are shear stress (from FaSTMECH) and bed surface geometric mean grain size (from the automated image analysis) for four locations along the y = 0.8 m profile. The arrows show the general pattern in the downstream direction along the y = 0.8 m profile, whereas the dashed line shows the actual trajectory along the profile.

lateral sediment transport driven by topographically induced cross-stream shear stress (Figure 6b) reduces the amount of sediment transport necessary to maintain steady conditions. Because the shear stress at x = 23 m is virtually the same as that at x = 18.5 m, this reduced sediment transport is achieved through bed coarsening (this is further elucidated in the following paragraph). From x = 23 m to x = 29.25 m, the shear stress declines dramatically due to thinning of the flow and flattening of the water surface slope associated with the slowing and shoaling of the flow around the bar such that essentially no sediment transport is occurring on the top of the bar, and by this point all of the sediment that was being transported upstream has been transported laterally so that it is accommodated by flux through the pool. From x = 30 m to x = 41 m, the boundary shear stress increases, and here there is a lateral sediment influx driven by cross-stream component of the shear stress oriented toward the left bank (Figure 6b). Here convergence of boundary shear stress is balanced by convergence in sediment transport, and the bed accommodates this increasing sediment flux by becoming finer.

[44] The development of coarse bars and fine pools in our experiment suggests that, along a path moving up the bar, the material moving as cross-stream sediment transport became finer, preferentially shuttling fine sediment into the pools. Unfortunately, because our bed load samples were small, we are unable to present reliably accurate measurements of the grain size distribution of the bed load and therefore cannot experimentally verify that the cross-stream transport became finer along a profile progressing up the bar. However, *Parker* [1990] and *Wilcock and Crowe*'s [2003] mixed-grain size bed load transport models can be used to show how, theoretically, the cross-stream flux should be becoming more size selective. *Wilcock and McArdell* [1993] suggested that the ratio of the fraction of the ith grain size in the load, p_i, to the fraction of the ith grain size on the bed surface, F_i, can be used to assess whether the bed is in a state of full or partial mobility. If p_i/F_i is constant (i.e., equal to 1.0) for all grain sizes D_i, the system is in a state of perfect surface-based equal mobility [*Parker*, 2008]. However, when the ratio becomes smaller as grain size increases, the relative transport of coarse grains is reduced so that partial or selective transport is occurring, or that fine grain size fractions were transported at rates higher than proportionally represented on the bed surface (perhaps due to high supply of fine material), giving the appearance of a cascading trend. Greater deviations from constant p_i/F_i indicate more size-selective conditions.

[45] To explore this for our experiment, we used the FaSTMECH-computed boundary shear stress and the observed (from automated image analysis) bed grain size distribution to calculate bed load transport from *Parker* [1990] and *Wilcock and Crowe*'s [2003] formulas. The algorithms use the shear stress and bed surface grain size distribution as inputs to compute the total transport rate q_T and the grain size distribution of the load p_i, which can then be used with the local bed surface grain size distribution F_i to compute p_i/F_i for each grain size D_i. This type of analysis normally compares conditions of partial versus equal mobility per grain size fraction at different flow levels [e.g., *Wilcock and McArdell*, 1993; *Clayton and Pitlick*, 2007], whereas for this study, transport conditions are compared spatially, over changes in x. Figure 10 shows computed p_i/F_i plots for selected distances downstream along the y = 0.8 m transect where the bed surface is coarser than the median size of the bed material (11 mm). Both transport expressions predict that where the boundary shear stress is relatively low compared to the observed grain size of the surface (x = 26 and 30 m in Figure 10) that deviation from equal mobility is greatest and conversely where the boundary shear stress is relatively large compared to the surface grain size (x = 20 and 37 m in Figure 10), equal mobility is more closely approximated (though not reached). This effect is more apparent in *Parker*'s [1990] algorithm than *Wilcock and Crowe*'s [2003] algorithm, particularly for coarse size fractions, perhaps because *Wilcock and Crowe*'s [2003] algorithm incorporates a more complex hiding function whose exponent is a function of D_i/D_g, and because it was developed with the intention of capturing mobilization effects of sand on coarse grains while our experimental conditions were sand-free. Nevertheless, where the boundary shear stress rapidly declines (as flow shoals over the top of the bar between x = 20 m and x = 30 m (Figures 2, 6, and 8) and the bed is coarse, both algorithms suggest that the strongest tendency to transport mostly the finer fraction occurs. Along this path the boundary shear stress is oriented toward the opposite bank (Figure 6b) and the mobilized finer sediment is transported across the channel away from the zone of decreasing boundary shear stress (Figure 6c). This suggests that the topographically induced divergence of boundary

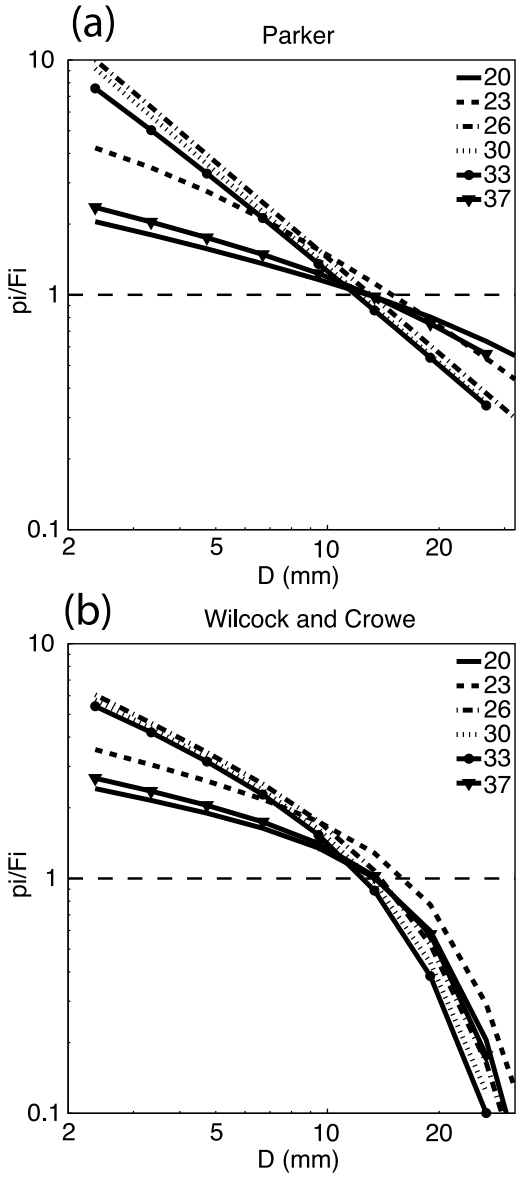

Figure 10. p_i/F_i ratios calculated by grain size for various x locations along the $y = 0.8$ m transect using (a) *Parker*'s [1990] and (b) *Wilcock and Crowe*'s [2003] bed load transport algorithms. The legend indicates the x position (in meters) for each line.

shear stress leads to differential mobilization of the finer sediment, coarsening of the bed and equilibrium topography, i.e., the formation of a forced bed-surface patch.

[46] Our interpretation is generally in agreement with *Lanzoni and Tubino*'s [1999] description of the implications of heterogeneous sediment on alternate bar formation, which emerged from their analytical stability analysis. Their theoretical results suggested that mixed-size sediments might appreciably inhibit bar migration, and that selective transport leads to coarse bars. The alternate bars that developed in *Lisle et al.*'s [1991, 1993] experiments also formed coarse bar tops and became stationary, which they attributed to bar head stabilization by coarse sediment and preferential incision in the pools. Our bars formed sorting patterns similar to those of *Lisle et al.* [1991, 1993], but it is difficult to determine precisely why our bars stopped growing and migrating since, in addition to strong sorting, the upstream bar's location was forced by a physical constriction of the flow at the flume inlet.

[47] Field studies of surface sorting on channel beds suggests that channel curvature can play a role of varying importance for bed sorting patterns. Studies of straight (or nearly straight) reaches with bars in gravel bed rivers have generally documented surface sorting patterns of coarse bar tops and fine pools [e.g., *Mosley and Tindale*, 1985; *Kinerson*, 1990; *Lisle and Hilton*, 1992; *Lisle and Madej*, 1992]. However, field observations of channel bends with point bars tend to document the opposite pattern of fine bars and coarse pools [*Bluck*, 1971; *Bridge and Jarvis*, 1976, 1982; *Bluck*, 1987; *Whiting and Dietrich*, 1991; *Laronne and Duncan*, 1992; *Carson*, 1986; *Clayton and Pitlick*, 2008; *Clayton*, 2010]. Point bars in curved channels [e.g., *Bluck*, 1971], alternate bars in straight channels [e.g., *Lisle and Madej*, 1992] and unit bars [e.g., *Lunt and Bridge*, 2004] all exhibit slight downstream fining along the bar.

[48] The contradictory sorting patterns observed in straight and curved channels suggests that the presence of curvature induces a shift in the dominant sorting mechanism. In bends, channel curvature creates a strong secondary circulation directed inward at the bed, toward the point bar [*Smith and McLean*, 1984]. For example, following *Parker and Andrews* [1985], *Lanzoni and Tubino* [1999] suggest that cross-stream sediment flux, $q_{i,n}$, can be expressed as:

$$q_{i,n} = |\mathbf{q}_i|\left\{\sin\chi - \frac{r}{\beta}\left[\frac{1}{\tau_g^*} f_h\left(\frac{D_i}{D_g}\right)\right]^{1/2}\frac{\partial\eta}{\partial n}\right\}. \tag{9}$$

Here $\mathbf{q}_i$ is the sediment flux vector of the ith grain size computed by, say, *Parker*'s [1990] model, χ is the angle the boundary shear stress vector makes with the s axis, β is the width to depth ratio, τ_g^* is the Shields stress computed for D_g, f_h (D_i/D_g) is a reduced hiding function, $\partial\eta/\partial n$ is the cross-stream bed slope, and r is a parameter that varies from 0.5 to 1.5. The term on the right-hand side inside the braces represents the effects of friction, lateral bed topography, and hiding effects. The sin χ term represents the effects of the transverse component of velocity and the effects of curvature-induced secondary circulations. *Blondeaux and Seminara* [1985] suggested that sin χ can be expressed as:

$$\sin\chi = \frac{v}{(u^2+v^2)^{1/2}} - a\frac{h}{r_0+n}, \tag{10}$$

where u and v are the components of the velocity vector in the s and n directions, h is the flow depth, r_o is the radius of curvature, and a is a scaling parameter ranging from 7 to 12 [e.g., *Engelund*, 1974; *Allen*, 1978; *Bridge and Jarvis*, 1982; *Dietrich and Smith*, 1983]. In straight channels, the $h/(r_0 + n)$ term is zero, but in bends it can become quite important. This secondary circulation is opposed by the outward gravitational force on particles provided by the cross-stream slope of the point bar. For fine particles, the effect of the secondary circulation exceeds the gravitational force, causing them to be preferentially transported into a reduced shear stress zone over the bar and transported away. Larger particles, however,

roll downslope into the higher shear stress zone in the pool [*Parker and Andrews*, 1985; *Clayton and Pitlick*, 2007]. Curvature effects may be less important in straight channels, which should have weaker secondary circulations and will develop coarse bars and fine pools because the finer sediment is preferentially transported laterally away from the bar via topographic steering.

[49] The actual importance of curvature on bed sediment sorting for particular location will of course depend on the details of local channel plan form, bed topography, and flow regime. Local sorting also is tightly coupled to the details of the bar shape, since the shape of the bar will determine where flow accelerations or decelerations, and consequently shear stress increases or decreases, occur. The shape of our bars resulted in flow deceleration over the bar top, but it is possible that had the upstream end of our bar been wider, the flow could have accelerated and the stress could have increased over the bar, resulting in a different bed surface sorting pattern [e.g., *Whiting and Dietrich*, 1991].

[50] Unlike gravel bedded channels, sediment transport in sand-bedded channels typically occurs under high excess shear stress conditions in which all grain sizes are fully mobile [*Parker*, 2008]. In these channels, one would expect the coarse sediment to track the zone of highest shear stress, so even relatively straight, alternate bar reaches should have fine bars and coarse pools [*Dietrich and Smith*, 1984].

5. Conclusions

[51] Observations of the surface texture of gravel bed rivers generally indicate that in curved channels the point bar is finer than the adjacent pool, in straight channels alternate bars are coarser than pools, and bars in both straight and curved channels tend to have a coarse to fine texture gradient along the bar top in the downstream direction. Our experiment shows how this pattern of forced bed surface patchiness is a consequence of interactions between channel topography, the flow field, and the sediment transport field.

[52] In our experiment, we developed bed topography and a pattern of forced bed surface patchiness similar to the field case of a straight channel with alternate bars. Our channel reached quasi-steady conditions with an overall sorting pattern of coarse bar tops and fine pools. This pattern did not track the calculated boundary shear stress field; that is, the coarse bar top was not an area of high boundary shear stress and the fine pool bed was not an area of low boundary shear stress.

[53] The development of alternate bars in our channel produced a spatially variable shear stress field. Thinning and shoaling of the flow over the bar caused the stress over the bar to decrease and flow convergence in the pool produced locally high boundary shear stress there. Sediment was transported laterally off of the bar and into the pool due to the cross-stream component of the flow field. This lateral transport became increasingly size-selective toward the downstream end of the bar as the shear stress on the bar declined, and it caused the local sediment supply along the bar to progressively decrease, which was accommodated locally through bed surface coarsening. Downstream of the bar, an influx of lateral sediment supply due to local stress convergence allowed the bed to fine. Thus, topographically forced divergences in the boundary shear stress field are matched by divergences in the sediment transport field, which in turn were accommodated by changes in bed surface texture allowing the channel to maintain quasi-steady state conditions.

Notation

a scaling parameter for helical flow.
A parameter relating grain size to roughness height.
D grain size.
D_{50}, D_{84} grain size for which 50 and 84% of the grain size distribution is finer.
D_g geometric mean bed surface grain size.
F_i fraction of the ith grain size on the bed surface.
f_{li} fraction of the ith grain size transferred between the surface and the subsurface during aggradation or degradation.
f_h lateral hiding function.
g gravitational acceleration.
h flow depth.
L_a active layer thickness.
n cross-stream coordinate (channel fitted).
$q_{i,n}$ cross-stream sediment flux per unit width of the ith grain size fraction.
$q_{i,s}$ downstream sediment flux per unit width of the ith grain size fraction.
q_n cross-stream sediment flux per unit width.
q_s downstream sediment flux per unit width.
Q_n total cross-stream sediment flux.
Q_s total downstream sediment flux.
r frictional parameter.
r_0 radius of curvature.
s downstream coordinate (channel-fitted).
t time.
u downstream velocity.
u_* shear velocity.
v cross-stream velocity.
W channel width.
x downstream coordinate (Cartesian).
y cross-stream coordinate (Cartesian).
z height above the bed.
z_0 roughness height.
β width-to-depth ratio.
χ angle the boundary shear stress vector makes with the s axis.
η bed elevation.
κ von Karman's constant.
λ_p bed porosity.
ρ water density.
ρ_s sediment density.
σ geometric standard deviation.
τ boundary shear stress.
τ^* nondimensional Shields stress.
τ_c^* Shields number for initial motion.
τ_g^* nondimensional Shields stress computed with D_g.

[54] **Acknowledgments.** This work was supported financially by the National Center for Earth-surface Dynamics and by a National Science Foundation Graduate Research Fellowship (to P.A.N.). Jeff Marr provided critical assistance during the experiments, and the large group of staff and researchers involved with the Streamlab06 project were very helpful. This

work also benefited from discussions with Christian Braudrick, Toby Minear, Stefano Lanzoni, and Giovanni Seminara. Carl Legleiter provided very useful code that helped in processing FaSTMECH output. Constructive reviews from two anonymous reviewers, Jonathan Nelson, and Associate Editor John Pitlick improved the clarity of the manuscript.

References

Allen, J. R. L. (1978), L. Van Bendegom: A neglected innovator in meander studies, *Mem. Can. Soc. Pet. Geol.*, *5*, 199–209.

Andrews, E. D., and D. C. Erman (1986), Persistence in the size distribution of surficial bed material during an extreme snowmelt flood, *Water Resour. Res.*, *22*(2), 191–197, doi:10.1029/WR022i002p00191.

Bathurst, J. C. (2002), At-a-site variation and minimum flow resistance for mountain rivers, *J. Hydrol. Amsterdam*, *269*(1–2), 11–26, doi:10.1016/S0022-1694(02)00191-9.

Best, J. L. (1996), The fluid dynamics of small-scale alluvial bedforms, in *Advances in Fluvial Dynamics and Stratigraphy*, edited by P. A. Carling and M. R. Dawson, pp. 67–125, John Wiley, Chichester, U. K.

Blondeaux, P., and G. Seminara (1985), A unified bar-bend theory of river meanders, *J. Fluid Mech.*, *157*, 449–470, doi:10.1017/S0022112085002440.

Bluck, B. J. (1971), Sedimentation in the meandering River Endrick, *Scott. J. Geol.*, *7*, 93–138, doi:10.1144/sjg07020093.

Bluck, B. J. (1987), Bed forms and clast size changes in gravel-bed rivers, in *River Channels: Environment and Process*, *Inst. Br. Geogr. Spec. Publ.*, vol. 18, edited by K. Richards, pp. 159–178, Blackwell Sci., Oxford, U. K.

Bridge, J. S. (1977), Flow, bed topography, grain size and sedimentary structure in bends: A three dimensional model, *Earth Surf. Processes*, *2*, 401–416, doi:10.1002/esp.3290020410.

Bridge, J. S. (1992), A revised model for water flow, sediment transport, bed topography and grain size sorting in natural river bends, *Water Resour. Res.*, *28*(4), 999–1013, doi:10.1029/91WR03088.

Bridge, J. S., and J. Jarvis (1976), Flow and sedimentary processes in the meandering river South Esk, Glen Clova, Scotland, *Earth Surf. Processes*, *1*, 303–336, doi:10.1002/esp.3290010402.

Bridge, J. S., and J. Jarvis (1982), The dynamics of a river bend: A study in flow and sedimentary processes, *Sedimentology*, *29*(4), 499–541, doi:10.1111/j.1365-3091.1982.tb01732.x.

Buffington, J. M., and D. R. Montgomery (1999a), A procedure for classifying textural facies in gravel-bed rivers, *Water Resour. Res.*, *35*(6), 1903–1914, doi:10.1029/1999WR900041.

Buffington, J. M., and D. R. Montgomery (1999b), Effects of sediment supply on surface textures of gravel-bed rivers, *Water Resour. Res.*, *35*(11), 3523–3530, doi:10.1029/1999WR900232.

Buffington, J. M., and D. R. Montgomery (1999c), Effects of hydraulic roughness on surface textures of gravel-bed rivers, *Water Resour. Res.*, *35*(11), 3507–3521, doi:10.1029/1999WR900138.

Buffington, J. M., D. R. Montgomery, and H. M. Greenberg (2004), Basin-scale availability of salmonid spawning gravel as influenced by channel type and hydraulic roughness in mountain catchments, *Can. J. Fish. Aquat. Sci.*, *61*(11), 2085–2096, doi:10.1139/f04-141.

Bunte, K., and S. R. Abt (2001), Sampling surface and subsurface particle-size distributions in wadable gravel- and cobble-bed streams for analyses in sediment transport, hydraulics, and streambed monitoring, *Gen. Tech. Rep. RMRS-GTR-74*, U.S. Dep. of Agric., For. Serv., Rocky Mt. Res. Stn., Fort Collins, Colo.

Carson, M. A. (1986), Characteristics of high-energy "meandering" rivers; the Canterbury Plains, New Zealand, *Bull, Mem. Geol. Soc. Am.*, *97*(7), 886–895, doi:10.1130/0016-7606(1986)97<886:COHMRT>2.0.CO;2.

Clayton, J. A. (2010), Local sorting, bend curvature, and particle mobility in meandering gravel bed rivers, *Water Resour. Res.*, *46*, W02601, doi:10.1029/2008WR007669.

Clayton, J. A., and J. Pitlick (2007), Spatial and temporal variations in bed load transport intensity in a gravel bed river bend, *Water Resour. Res.*, *43*, W02426, doi:10.1029/2006WR005253.

Clayton, J. A., and J. Pitlick (2008), Persistence of the surface texture of a gravel-bed river during a large flood, *Earth Surf. Processes Landforms*, *33*(5), 661–673, doi:10.1002/esp.1567.

Colombini, M., G. Seminara, and M. Tubino (1987), Finite-amplitude alternate bars, *J. Fluid Mech.*, *181*, 213–232, doi:10.1017/S0022112087002064.

Crowder, D. W., and P. Diplas (1997), Sampling heterogeneous deposits in gravel-bed streams, *J. Hydraul. Eng.*, *123*(12), 1106–1117, doi:10.1061/(ASCE)0733-9429(1997)123:12(1106).

Dietrich, W. E. (1987), Mechanics of flow and sediment transport in river bends, in *River Channels: Environment and Process*, *Inst. Br. Geogr. Spec. Publ.*, vol. 18, edited by K. S. Richards, pp. 179–227, Blackwell Sci., Oxford, U. K.

Dietrich, W. E., and J. D. Smith (1983), Influence of the point bar on flow through curved channels, *Water Resour. Res.*, *19*(5), 1173–1192, doi:10.1029/WR019i005p01173.

Dietrich, W. E., and J. D. Smith (1984), Bed load transport in a river meander, *Water Resour. Res.*, *20*(10), 1355–1380, doi:10.1029/WR020i010p01355.

Dietrich, W. E., and P. Whiting (1989), Boundary shear stress and sediment transport in river meanders of sand and gravel, in *River Meandering*, *Water Resour. Monogr.*, vol. 12, edited by S. Ikeda and G. Parker, pp. 1–50, AGU, Washington, D. C.

Dietrich, W. E., J. W. Kirchner, H. Ikeda, and F. Iseya (1989), Sediment supply and the development of the coarse surface layer in gravel-bedded rivers, *Nature*, *340*, 215–217, doi:10.1038/340215a0.

Dietrich, W. E., P. A. Nelson, E. Yager, J. G. Venditti, M. P. Lamb, and L. Collins (2005), Sediment patches, sediment supply, and channel morphology, in *4th Conference on River, Coastal, and Estuarine Morphodynamics, RCEM 2005*, edited by G. Parker and M. H. Garcia, pp. 79–90, A. A. Balkema, Rotterdam, Germany.

Engelund, F. (1974), Flow and bed topography in channel bends, *J. Hydraul. Div. Am. Soc. Civ. Eng.*, *100*, 1631–1648.

Forbes, D. L. (1983), Morphology and sedimentology of a sinuous gravel-bed channel system: lower Babbage River, Yukon coastal plain, Canada, in *Modern and Ancient Fluvial Systems*, edited by J. D. Collinson and J. Lewin, pp. 195–206, doi:10.1002/9781444303773.ch15, Blackwell Sci, Oxford, U. K.

Garcia, C., J. B. Laronne, and M. Sala (1999), Variable source areas of bedload in a gravel-bed stream, *J. Sediment. Res.*, *69*(1), 27–31.

Gilbert, G. K. (1914), The transportation of debris by running water, *U.S. Geol. Surv. Prof. Pap.*, *86*, 263 pp.

Graham, D. J., I. Reid, and S. P. Rice (2005a), Automated sizing of coarse-grained sediments: Image-processing procedures, *Math. Geol.*, *37*(1), 1–28, doi:10.1007/s11004-005-8745-x.

Graham, D. J., S. P. Rice, and I. Reid (2005b), A transferable method for the automated grain sizing of river gravels, *Water Resour. Res.*, *41*, W07020, doi:10.1029/2004WR003868.

Graham, D. J., S. P. Rice, and I. Reid (2005c), Comment: Photographic techniques for characterizing streambed particle sizes, *Trans. Am. Fish. Soc.*, *134*, 1599–1603, doi:10.1577/T04-146.1.

Graham, D. J., A.-J. J. Rollet, H. Piégay, and S. P. Rice (2010), Maximizing the accuracy of image-based surface sampling techniques, *Water Resour. Res.*, *46*, W02508, doi:10.1029/2008WR006940.

Harrison, L. R., and E. A. Keller (2007), Modeling forced pool-riffle hydraulics in a boulder-bed stream, southern California, *Geomorphology*, *83*(3–4), 232–248, doi:10.1016/j.geomorph.2006.02.024.

Heritage, G. L., and D. J. Milan (2004), A conceptual model of the role of excess energy in the maintenance of a riffle-pool sequence, *Catena*, *58*(3), 235–257, doi:10.1016/j.catena.2004.05.002.

Hirano, M. (1971), River bed degradation with armouring, *Trans. Jpn. Soc. Civ. Eng*, *195*, 55–65.

Hubbard, E. F. (1988), Approval of standard rating for polymer-rotor pygmy meter with cat-whisker head (P-Pygmy or PPG Meter), *U.S. Geol. Suv. Off. Surf. Water Tech. Memo., 89-01*.

Ikeda, H. (1983), Experiments on bedload transport, bed forms, and sedimentary structures using fine gravel in the 4-meter-wide flume, *Environ. Res. Cent. Pap. 2*, Univ. of Tsukuba, Tsukuba, Japan.

Ikeda, S. (1989), Sediment transport and sorting at bends, in *River Meandering*, *Water Resour. Monogr.*, vol. 12, edited by S. Ikeda and G. Parker, pp. 3–125, AGU, Washington, D. C.

Jackson, R. G. (1975), Velocity-bed-form-texture patterns of meander bends in the lower Wabash River of Illinois and Indiana, *Geol. Soc. Am. Bull.*, *86*(11), 1511–1522, doi:10.1130/0016-7606(1975)86<1511:VPOMBI>2.0.CO;2.

Katul, G., P. Wiberg, J. Albertson, and G. Hornberger (2002), A mixing layer theory for flow resistance in shallow streams, *Water Resour. Res.*, *38*(11), 1250, doi:10.1029/2001WR000817.

Keller, E. A. (1971), Areal sorting of bed-load material: The hypothesis of velocity reversal, *Bull. Geol. Soc. Am.*, *82*(3), 753–756, doi:10.1130/0016-7606(1971)82[753:ASOBMT]2.0.CO;2.

Kellerhals, R., and D. I. Bray (1971), Sampling procedures for coarse fluvial sediments, *J. Hydraul. Div. Am. Soc. Civ. Eng.*, *97*(8), 1165–1180.

Kikkawa, H., S. Ikeda, and A. Kitagawa (1976), Flow and bed topography in curved open channels, *J. Hydraul. Div. Am. Soc. Civ. Eng.*, *102*, 1327–1342.

Kinerson, D. (1990), Surface response to sediment supply, M.S. thesis, Univ. of Calif., Berkeley.

Kinzel, P. J., J. M. Nelson, and A. K. Heckman (2009), Response of sandhill crane (*Grus canadensis*) riverine roosting habitat to changes in stage and sandbar morphology, *River Res. Appl.*, *25*(2), 135–152, doi:10.1002/rra.1103.

Lane, E. W. (1955), Design of stable channels, *Trans. Am. Soc. Civ. Eng.*, *120*, 1234–1260.

Lane, S. N., K. F. Bradbrook, K. S. Richards, P. A. Biron, and A. G. Roy (1999), The application of computational fluid dynamics to natural river channels: Three-dimensional versus two-dimensional approaches, *Geomorphology*, *29*(1–2), 1–20, doi:10.1016/S0169-555X(99)00003-3.

Lanzoni, S. (2000), Experiments on bar formation in a straight flume: 2. Graded sediment, *Water Resour. Res.*, *36*(11), 3351–3364, doi:10.1029/2000WR900161.

Lanzoni, S., and M. Tubino (1999), Grain sorting and bar instability, *J. Fluid Mech.*, *393*, 149–174, doi:10.1017/S0022112099005583.

Laronne, J., and M. Duncan (1992), Bedload transport paths and gravel bar formation, in *Dynamics of Gravel-bed Rivers*, edited by P. Billi, R. Hey, C. Thorne, and P. Tacconi, pp. 177–202, John Wiley, Chichester, U. K.

Laronne, J. B., C. Garcia, and I. Reid (2000), Mobility of patch sediment in gravel bed streams: Patch character and its implications for bedload, in *Gravel-Bed Rivers V*, edited by M. P. Mosley, pp. 249–280, N. Z. Hydrol. Soc., Wellington.

Leopold, L. B., and M. G. Wolman (1957), River channel patterns: Braided, meandering and straight, *U.S. Geol. Surv. Prof. Pap.*, *282*, 39–85.

Leopold, L. B., and M. G. Wolman (1960), River meanders, *Geol. Soc. Am. Bull.*, *71*(6), 769–793, doi:10.1130/0016-7606(1960)71[769:RM]2.0.CO;2.

Lisle, T. E. (1979), A sorting mechanism for a riffle-pool sequence, *Geol. Soc. Am. Bull.*, *90*(2), 1142–1157.

Lisle, T. E., and S. Hilton (1992), Volume of fine sediment in pools: An index of sediment supply in gravel-bed streams, *Water Resour. Bull.*, *28*(2), 371–383.

Lisle, T. E., and S. Hilton (1999), Fine bed material in pools of natural gravel bed channels, *Water Resour. Res.*, *35*(4), 1291–1304, doi:10.1029/1998WR900088.

Lisle, T., and M. Madej (1992), Spatial variation in armouring in a channel with high sediment supply, in *Dynamics of Gravel-bed Rivers*, edited by P. Billi et al., pp. 277–293, John Wiley, Chichester, U. K.

Lisle, T. E., H. Ikeda, and F. Iseya (1991), Formation of stationary alternate bars in a steep channel with mixed-size sediment: A flume experiment, *Earth Surf. Processes Landforms*, *16*(5), 43–469, doi:10.1002/esp.3290160507.

Lisle, T. E., F. Iseya, and H. Ikeda (1993), Response of a channel with alternate bars to a decrease in supply of mixed-size bed load: A flume experiment, *Water Resour. Res.*, *29*(11), 3623–3629, doi:10.1029/93WR01673.

Lisle, T. E., J. M. Nelson, J. Pitlick, M. A. Madej, and B. L. Barkett (2000), Variability of bed mobility in natural, gravel-bed channels and adjustments to sediment load at local and reach scales, *Water Resour. Res.*, *36*(12), 3743–3755, doi:10.1029/2000WR900238.

Lunt, I. A., and J. S. Bridge (2004), Evolution and deposits of a gravelly braid bar, Sagavanirktok River, Alaska, *Sedimentology*, *51*(3), 415–432, doi:10.1111/j.1365-3091.2004.00628.x.

MacWilliams, M. L., J. M. Wheaton, G. B. Pasternack, R. L. Street, and P. K. Kitanidis (2006), Flow convergence routing hypothesis for pool-riffle maintenance in alluvial rivers, *Water Resour. Res.*, *42*, W10427, doi:10.1029/2005WR004391.

Marr, J. D., S. R. Johnson, C. Hill, and C. Ellis (2010), StreamLab06: Overview of experiments, instrumentation, and data collection, *Proj. Rep. 539*, Natl. Cent. for Earth Surf. Dyn., St. Anthony Falls Lab., Univ. of Minn., Minneapolis.

McDonald, R. R., J. M. Nelson, and J. P. Bennett (2005), Multidimensional surface-water modeling system user's guide, *U.S. Geol. Surv. Tech. Meth.*, *6-B2*, 136 pp.

McEwan, I. K., T. M. Sheen, G. J. Cunningham, and A. R. Allen (2000), Estimating the size composition of sediment surfaces through image analysis, *Proc. Inst. Civ. Eng. Water Mar. Eng.*, *142*(4), 189–195.

Milan, D. J., G. L. Heritage, A. R. G. Large, and M. E. Charlton (2001), Stage-dependent variability in tractive force distribution through a riffle-pool sequence, *Catena*, *44*(2), 85–109, doi:10.1016/S0341-8162(00)00155-7.

Mosley, M. P., and D. S. Tindale (1985), Sediment variability and bed material sampling in gravel-bed rivers, *Earth Surf. Processes Landforms*, *10*(5), 465–482, doi:10.1002/esp.3290100506.

Nelson, J. M., and R. R. McDonald (1995), Mechanics and modeling of flow and bed evolution in lateral separation eddies, report, 39 pp., U.S. Geol. Surv. Grand Canyon Monit. and Res. Cent., Flagstaff, Ariz.

Nelson, J. M., and J. D. Smith (1989), Flow in meandering channels with natural topography, in *River Meandering*, *Water Resour. Monogr.*, vol. 12, edited by S. Ikeda and G. Parker, pp. 69–102, AGU, Washington, D. C.

Nelson, J. M., J. P. Bennett, and S. M. Wiele (2003), Flow and sediment-transport modeling, in *Tools in Fluvial Geomorphology*, edited by G. M. Kondolf and H. Piégay, pp. 539–576, John Wiley, Chichester, U. K.

Nelson, P. A., J. G. Venditti, W. E. Dietrich, J. W. Kirchner, H. Ikeda, F. Iseya, and L. S. Sklar (2009), Response of bed surface patchiness to reductions in sediment supply, *J. Geophys. Res.*, *114*, F02005, doi:10.1029/2008JF001144.

Paola, C., and R. Seal (1995), Grain size patchiness as a cause of selective deposition and downstream fining, *Water Resour. Res.*, *31*(5), 1395–1408, doi:10.1029/94WR02975.

Parker, G. (1990), Surface-based bedload transport relation for gravel rivers, *J. Hydraul. Res.*, *28*(4), 417–436, doi:10.1080/00221689009499058.

Parker, G. (2008), Transport of gravel and sediment mixtures, in *Sedimentation Engineering*, *ASCE Man.*, vol. 110, edited by M. H. Garcia and G. Parker, pp. 165–252, Am. Soc. Civ. Eng., Reston, Va.

Parker, G., and E. D. Andrews (1985), Sorting of bed load sediment by flow in meander bends, *Water Resour. Res.*, *21*(9), 1361–1373, doi:10.1029/WR021i009p01361.

Parker, G., and P. C. Klingeman (1982), On why gravel bed streams are paved, *Water Resour. Res.*, *18*(5), 1409–1423, doi:10.1029/WR018i005p01409.

Parker, G., P. R. Wilcock, C. Paola, W. E. Dietrich, and J. Pitlick (2007), Physical basis for quasi-universal relations describing bankfull hydraulic geometry of single-thread gravel bed rivers, *J. Geophys. Res.*, *112*, F04005, doi:10.1029/2006JF000549.

Pitlick, J. (1988), Variability of bed load measurement, *Water Resour. Res.*, *24*(1), 173–177, doi:10.1029/WR024i001p00173.

Power, M. E., W. E. Dietrich, and K. O. Sullivan (1998), Experimentation, observation, and inference in river and watershed investigations, in *Experimental Ecology*, edited by W. J. Resetarits and J. Bernardo, pp. 113–132, Oxford Univ. Press, New York.

Rattray, M., Jr., and E. Mitsuda (1974), Theoretical analysis of conditions in a salt wedge, *Estuarine Coastal Mar. Sci.*, *2*, 375–394, doi:10.1016/0302-3524(74)90006-1.

Sambrook Smith, G. H., and R. I. Ferguson (1995), The gravel sand transition along river channels, *J. Sediment. Res.*, *65*(2), 423–430.

Sawyer, A. M., G. B. Pasternack, H. J. Moir, and A. A. Fulton (2010), Riffle-pool maintenance and flow convergence routing observed on a large gravel-bed river, *Geomorphology*, *114*(3), 143–160, doi:10.1016/j.geomorph.2009.06.021.

Sime, L. C., R. I. Ferguson, and M. Church (2007), Estimating shear stress from moving boat acoustic Doppler velocity measurements in a large gravel bed river, *Water Resour. Res.*, *43*, W03418, doi:10.1029/2006WR005069.

Singh, A., K. Fienberg, D. J. Jerolmack, J. Marr, and E. Foufoula-Georgiou (2009), Experimental evidence for statistical scaling and intermittency in sediment transport rates, *J. Geophys. Res.*, *114*, F01025, doi:10.1029/2007JF000963.

Smith, J. D., and S. R. McLean (1984), A model for flow in meandering streams, *Water Resour. Res.*, *20*(9), 1301–1315, doi:10.1029/WR020i009p01301.

Sun, T., P. Meakin, and T. Jøssang (2001a), A computer model for meandering rivers with multiple bed load sediment sizes: 1. Theory, *Water Resour. Res.*, *37*(8), 2227–2242, doi:10.1029/2000WR900396.

Sun, T., P. Meakin, and T. Jøssang (2001b), A computer model for meandering rivers with multiple bed load sediment sizes: 2. Computer simulations, *Water Resour. Res.*, *37*(8), 2243–2258, doi:10.1029/2000WR900397.

Thompson, D. M., and K. S. Hoffman (2001), Equilibrium pool dimensions and sediment-sorting patterns in coarse-grained, New England channels, *Geomorphology*, *38*(3–4), 301–316, doi:10.1016/S0169-555X(00)00100-8.

Thompson, D. M., E. E. Wohl, and R. D. Jarrett (1996), A revised velocity-reversal and sediment-sorting model for a high-gradient, pool-riffle stream, *Phys. Geogr.*, *17*(2), 142–156.

Thompson, D. M., E. E. Wohl, and R. D. Jarrett (1999), Velocity reversals and sediment sorting in pools and riffles controlled by channel constrictions, *Geomorphology*, *27*(3–4), 229–241, doi:10.1016/S0169-555X(98)00082-8.

U.S. Bureau of Reclamation (2001), *Water Measurement Manual*, 317 pp., U.S. Gov. Print. Off., Washington, D. C.

Vincent, L., and P. Soille (1991), Watersheds in digital spaces: An efficient algorithm based on immersion simulations, *IEEE Trans. Pattern Anal. Mach. Intell.*, *13*(6), 583–598, doi:10.1109/34.87344.

Whiting, P. J. (1996), Sediment sorting over bed topography, in *Advances in Fluvial Dynamics and Stratigraphy*, edited by P. Carling and M. Dawson, pp. 204–228, John Wiley, Chichester, U. K.

Whiting, P. J., and W. E. Dietrich (1990), Boundary shear stress and roughness over mobile alluvial beds, *J. Hydraul. Eng.*, *116*(12), 1495–1511, doi:10.1061/(ASCE)0733-9429(1990)116:12(1495).

Whiting, P. J., and W. E. Dietrich (1991), Convective accelerations and boundary shear stress over a channel bar, *Water Resour. Res.*, *27*(5), 783–796, doi:10.1029/91WR00083.

Whiting, P. J., W. E. Dietrich, L. B. Leopold, T. G. Drake, and R. L. Shreve (1988), Bedload sheets in heterogeneous sediment, *Geology*, *16*(2), 105–108, doi:10.1130/0091-7613(1988)016<0105:BSIHS>2.3.CO;2.

Wiberg, P. L., and J. D. Smith (1991), Velocity distribution and bed roughness in high-gradient streams, *Water Resour. Res.*, *27*(5), 825–838, doi:10.1029/90WR02770.

Wilcock, P. R. (1996), Estimating local bed shear stress from velocity observations, *Water Resour. Res.*, *32*(11), 3361–3366, doi:10.1029/96WR02277.

Wilcock, P. R., and J. C. Crowe (2003), Surface-based transport model for mixed-size sediment, *J. Hydraul. Eng.*, *129*(2), 120–128, doi:10.1061/(ASCE)0733-9429(2003)129:2(120).

Wilcock, P. R., and B. T. DeTemple (2005), Persistence of armor layers in gravel-bed streams, *Geophys. Res. Lett.*, *32*, L08402, doi:10.1029/2004GL021772.

Wilcock, P. R., and B. W. McArdell (1993), Surface-based fractional transport rates: Mobilization thresholds and partial transport of a sand-gravel sediment, *Water Resour. Res.*, *29*(4), 1297–1312, doi:10.1029/92WR02748.

Wolcott, J., and M. Church (1991), Strategies for sampling spatially heterogeneous phenomena: The example of river gravels, *J. Sediment. Res.*, *61*(4), 534–543.

Yager, E. M. (2006), Prediction of sediment transport in steep, rough streams, Ph.D. thesis, Univ. of Calif., Berkeley.

Yarnell, S. M., J. F. Mount, and E. W. Larsen (2006), The influence of relative sediment supply on riverine habitat heterogeneity, *Geomorphology*, *80*(3–4), 310–324, doi:10.1016/j.geomorph.2006.03.005.

W. E. Dietrich and P. A. Nelson, Department of Earth and Planetary Science, University of California, 307 McCone Hall #4767, Berkeley, CA 94720, USA. (pnelson@berkeley.edu)

J. G. Venditti, Department of Geography, Simon Fraser University, 8888 University Dr., Burnaby, BC V5A 1S6, Canada.